ARL-TR-8443 ● AUG 2018

US Army Research Laboratory

Computational Investigation on the Wake Flow of a Hemispherical Parachute Canopy

by Joseph D Vasile

NOTICES

Disclaimers

The findings in this report are not to be construed as an official Department of the Army position unless so designated by other authorized documents.

Citation of manufacturer's or trade names does not constitute an official endorsement or approval of the use thereof.

Destroy this report when it is no longer needed. Do not return it to the originator.

ARL-TR-8443 ● AUG 2018

US Army Research Laboratory

Computational Investigation on the Wake Flow of a Hemispherical Parachute Canopy

by Joseph D Vasile
Weapons and Materials Research Directorate, ARL

REPORT DOCUMENTATION PAGE

Form Approved
OMB No. 0704-0188

1. REPORT DATE *(DD-MM-YYYY)*	2. REPORT TYPE	3. DATES COVERED (From - To)
August 2018	Technical Report	May 2016–April 2018

4. TITLE AND SUBTITLE
Computational Investigation on the Wake Flow of a Hemispherical Parachute Canopy

5a. CONTRACT NUMBER

5b. GRANT NUMBER

5c. PROGRAM ELEMENT NUMBER

6. AUTHOR(S)
Joseph D Vasile

5d. PROJECT NUMBER

5e. TASK NUMBER

5f. WORK UNIT NUMBER

7. PERFORMING ORGANIZATION NAME(S) AND ADDRESS(ES)
US Army Research Laboratory
ATTN: RDRL-WML-E
Aberdeen Proving Ground, MD 21005

8. PERFORMING ORGANIZATION REPORT NUMBER
ARL-TR-8443

9. SPONSORING/MONITORING AGENCY NAME(S) AND ADDRESS(ES)

10. SPONSOR/MONITOR'S ACRONYM(S)

11. SPONSOR/MONITOR'S REPORT NUMBER(S)

12. DISTRIBUTION/AVAILABILITY STATEMENT
Approved for public release; distribution is unlimited.

13. SUPPLEMENTARY NOTES

14. ABSTRACT
A computational investigation on a rigid and periodic oscillating hemispherical canopy at a Reynolds number equal to 30,000 was initially explored to compare to that of the archival experimental work of a water tunnel-tested flexible parachute canopy. The wake flow of the computational study was compared to experimental data. Specifically, the effect of an upstream payload, turbulence model (i.e., unsteady Reynolds-averaged Navier-Stokes [RANS] and several versions of Hybrid RANS-large eddy simulation models), canopy permeability, and prescribed oscillation of the canopy shape on the development of the flow structures in the wake were considered. The predicted drag coefficients for all configurations do not compare well to those of the flexible canopy; however, they match well to literature on rigid hemispherical cups. Modeling both upstream forebody and canopy motion was shown to be most effective in reducing the size and structure of the wake. Moreover, the time-averaged flow solution of the wake for the periodic oscillating canopy with an upstream forebody compared best to the wake of the flexible parachute canopy. Furthermore, the advanced turbulence models were able to resolve the flow structures present in the wake quite well. The results indicate that the dynamics associated with a flexible canopy directly affect the aerodynamic properties as well as wake flow. Future efforts will focus on fluid-structure interactions, specifically, simulating a flexible canopy through the use of a coupled fluid dynamics-structural dynamics code.

15. SUBJECT TERMS
unsteady CFD, hybrid RANS-LES, parachute wake flow, hemispherical cup, parachute canopy dynamics, rigid canopy

16. SECURITY CLASSIFICATION OF:			17. LIMITATION OF ABSTRACT	18. NUMBER OF PAGES	19a. NAME OF RESPONSIBLE PERSON
a. REPORT	b. ABSTRACT	c. THIS PAGE			Joseph D Vasile
Unclassified	Unclassified	Unclassified	UU	60	19b. TELEPHONE NUMBER (Include area code) (410) 306-1794

Contents

List of Figures

List of Tables

Acknowledgments

This work was supported in part by the Project Manager Soldier Protection and Individual Equipment, Program Executive Office Soldier, US Army, and a grant of high-performance computing time from the US Department of Defense (DOD) High Performance Computing Modernization program at the US Army Research Laboratory DOD Supercomputing Resource Center (DSRC), Aberdeen Proving Ground, Maryland, and the Navy DSRC, Stennis Space Center, Mississippi. The author would like to thank Dr James DeSpirito, US Army Research Laboratory, as well as Dr Paul Batten and the technical staff from Metacomp Technologies for their help and discussions both relating to this work and with regard to computational fluid dynamics fundamentals and techniques.

1. Introduction

Fluid-structure interactions (FSIs) are an emerging area of study in the field of fluid dynamics. In many applications, the effect of the surrounding fluid of a structure influencing its dynamics needs to be considered and understood to ensure that specific design characteristics (safety, performance, etc.) are met. One area that is highly sensitive to FSI effects is the aerodynamic decelerator system, specifically, the airdrop system, where highly deformable fabrics interact with unsteady wake airflow, affecting the dynamics and shape of the flexible canopy. The flow around parachutes has been studied extensively,[1] mainly on the development of advanced finite element modeling techniques, in order to correctly predict the structural dynamics of a flexible canopy throughout all stages of operation. Stein et al.,[2,3] Benney et al.,[4] and Tezduyar et al.[5,6] presented a parallel computational strategy to simulate the FSI for a round parachute. Their strategy used a stabilized space–time formulation of the time-dependent, 3-D Navier-Stokes equations of incompressible flows for the fluid dynamics, and a finite-element formulation derived from the principle of virtual work for the structural dynamics. Large deformations of the structure were handled in the computational domain by using an automatic meshing moving scheme. The iterative coupling approach was achieved through the transfer of FSI information between the fluid and structure at the canopy surface interface. The displacements and displacement rates from the structural dynamics solution were used for updating the mesh for the fluid dynamic solution; in return, the pressure contributions from the fluid dynamic solution were used to compute the distributed loads on the structural dynamics solver. The process continued until convergence of shape and pressure distribution were achieved. Sahu et al.[7] and Sahu and Benney[8] also implemented a similar strategy in which the fluid dynamics solution was manually coupled to a static structural code that predicted the canopy shape of the US Army T-10 and C-9 parachute systems, respectively. In addition to accurately predicting the shape of the canopy, it is equally important to accurately predict the flow field solution around the canopy. The wake flow field downstream of the canopy is highly unsteady, consisting of vortical structures that are shed downstream. In order to accurately predict the pressure distribution on the canopy surface, it is necessary to resolve the flow structures in the wake region, close the surface of the canopy.

The purpose of the current investigation is to further our understanding of the 3-D flow structures present in the wake of a parachute canopy in order to predict aerodynamic parameters accurately. Although there are many studies on measuring and predicting the global aerodynamic parameters (e.g., drag coefficient),[9,10] there are few studies focused on the development of the wake flow past the canopy.

Jenkins and Desabrais[11] measured the instantaneous velocity flow field behind a falling parachute during a drop test using planar Doppler velocimetry (PDV). Additionally, the flow inside rigid cups has been studied previously[12]; however, there are few investigations that study the near wake flow field of rigid cup-like canopies. McQuilling et al.[13] performed a computational investigation of flow around a rigid hemisphere at multiple pitch angles to compare predicted surface pressure coefficient with experimental data. The steady-state flow solution implemented a k-ϵ turbulence model to accurately predict the pressure near the surface of the canopy. The current computational investigation was performed in order to compare flow field solutions and results to that of the experimental investigations completed by Johari and Desabrais[14] and Desabrais and Johari.[15,16] The detailed experimental works studied the dynamics of a flexible canopy as well as the flow field structures, velocity profiles, and shedding frequencies in the near wake through the use of stereoscopic particle image velocimetry and single-element hot-film anemometer.

The current computational study implemented both a rigid and also a periodically oscillating hemispherical shell with dimensions equal to that of the average values obtained from the experiment of the flexible canopy.[14] The focus of the current work was to identify simulation parameters (e.g., turbulence model), canopy features (i.e., permeability and motion), and upstream geometry effects (i.e., instrumented forebody) that produced global flow features in the wake that matched best to the experiment. The natural step forward is to implement a coupled fluid dynamics-structural dynamics code to fully capture the FSIs and better predict the wake flow of parachute canopies.

2. Technical Approach

2.1 Geometry and Computational Domain

The computational investigation was performed to virtually simulate the water tunnel experiment of Johari and Desabrais.[14] The dimensions of the computational domain matched the dimensions of the water tunnel. The experiments were conducted in a water tunnel test section that had a 0.6-m^2 cross section and a length of 2.4 m. The computational domain used for all simulations was meshed with Multipurpose Intelligent Meshing Environment (MIME) from Metacomp Technologies[17] and is presented in Fig. 1.

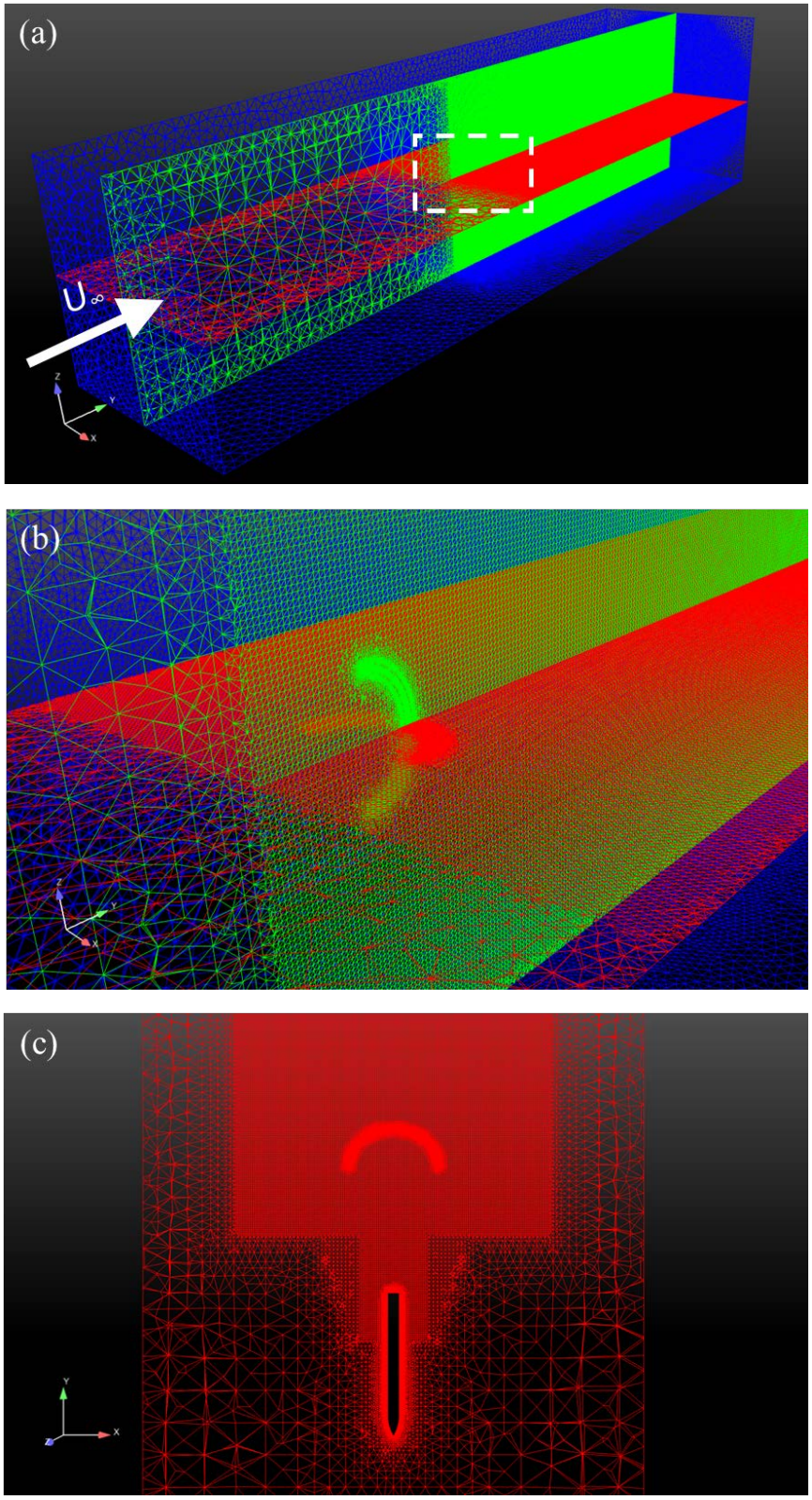

Fig. 1 Computational domain of a) water tunnel, b) zoomed in views near canopy only configuration, and c) forebody and canopy configuration

Three computational domains were used in the study. First, a single rigid hemispherical parachute canopy was modeled to suspend in the center of the modeled water tunnel test section. The base of the rigid canopy was placed at the center of the domain, with the origin defined as the center of the base. The dashed rectangle in Fig. 1a represents the location of a zoomed-in view that is presented in Fig. 1b. A mesh density cylinder was used to refine the mesh near the canopy as well as downstream in order to resolve wake eddies, which is necessary for large-eddy simulation (LES)-type solutions. The origin of the density box was aligned to the center of the canopy base, with a diameter equal to 0.6 m, beginning a diameter upstream of the canopy and spanning downstream until the end of the domain. The average cell size of the density box was approximately 0.006 m, or 5% of the diameter of the canopy base. The second computational domain addressed the effect of an upstream forebody (Fig. 1c). A forebody was positioned 0.22 m upstream of the hemispherical canopy in order to parallel the setup from the water tunnel experiment. A series of mesh density frustums and cylinders were implemented to refine the mesh to adequately resolve the flow structures near both forebody and canopy geometries. A set consisting of a mesh density frustum and a cylinder of equal diameter (0.75 canopy diameter) were placed two canopy diameters upstream, spanning downstream until aligned to a larger density cylinder beginning one canopy diameter upstream of the canopy base. The larger mesh density cylinder has a diameter of approximately 0.25 m and spans downstream until the end of the domain. The average cell size for each mesh density cylinder was approximately 0.003 m, or 2.5 % of the canopy base diameter. The third computational domain had identical parameters and density mesh regions that were used in the canopy and forebody domain; however, the canopy geometry was not included, and therefore not modeled. This computational domain was exclusively used for modeling the forebody to predict the drag and wake flow of the forebody without the presence of a canopy downstream. The forebody drag coefficient and wake flow were used to estimate the effect of the forebody on the drag coefficient of the canopy through an established empirical method, which is described in more detail in Section 3.1.2. The forebody and canopy geometries were resolved using a boundary layer mesh comprising a first cell wall spacing of prism layers set to 2.4×10^{-5} m to ensure y^+ values of 1 along both surfaces. The total mesh size for each computational domain was approximately 30-, 51-, and 45-M cells, respectively. Each domain consisted of triangular surface cells, with prism layers used along forebody and canopy surfaces, and predominantly tetrahedral cells for the rest of the domain.

2.1.1 Rigid Canopy and Forebody

The dimensions of the rigid canopy were selected based on the constructed diameter, $D_{0,}$ as well as the time-averaged projected base diameter measured from the experiment, D_p, of the flexible canopy during testing.[14] Moreover, the depth of the canopy, H, was selected based on the observed mean canopy depth of $H = 0.40\ D_p$. The rigid canopy was designed such that the hemispherical shape was tangent at the apex, as well as tangent near the skirt of the canopy. The thickness of the parachute was selected based on the thickness of the flexible fabric measured from the experiment, δ. Figure 2 and Table 1 show the schematics and geometry parameters of the rigid canopy used in the computational study, respectively.

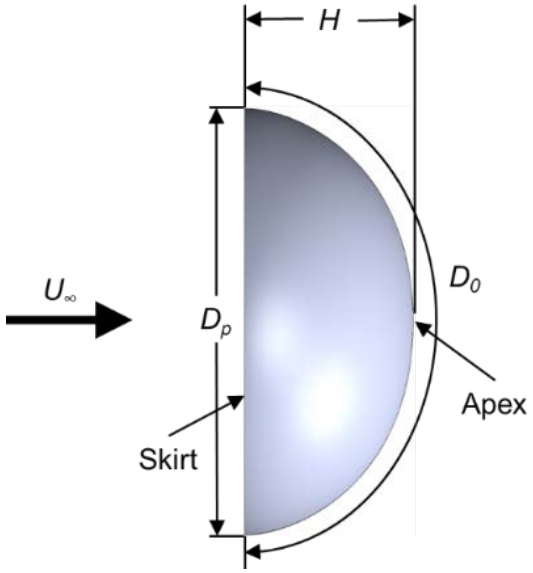

Fig. 2 Schematic of rigid canopy model

Table 1 Geometric parameters of rigid canopy

Parameter	D_0 (m)	D_p (m)	H (m)	Δ (m)	U_∞ (m/s)	Re_{Dp}
Rigid canopy	0.152	0.108	0.043	7.1×10^{-5}	0.22	30,000

In the experiment, the canopy was attached by 24 suspension lines to a stationary streamlined forebody. The forebody was supported by four rods in the center of the test section. Flow visualization from the experiment confirmed that the wake of the forebody support rods had a negligible effect on the parachute canopy geometry and dynamics. In the current computational study, the diameter, D_{fb}, and length, H_{fb}, of the forebody were defined based on the specifications from the water tunnel experiment. The specifications of the nose shape were inferred based on schematics of the experiment. The nose shape was selected to be approximately 10% of the

overall length of the forebody, with the base of the nose shape tangent to the forebody, tapering down to a sharp point. The forebody was placed, L (or 1 constructed canopy diameter, D_0), upstream from the base of the canopy, which was equal to the length of the suspension lines defined from the experiment. The wake of the suspension lines was assumed to be negligible and therefore was not modeled. Figure 3 and Table 2 show the schematics and geometry parameters of the forebody used in the computational study, respectively.

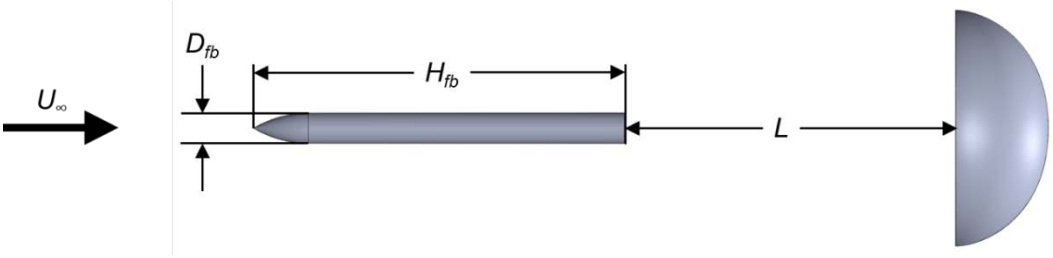

Fig. 3 Schematic of forebody and rigid canopy model

Table 2 Geometric parameters of forebody

Parameter	D_{fb} (m)	H_{fb} (m)	L (m)
Forebody	0.014	0.17	0.152

2.1.2 Periodic Oscillating Canopy

As was discussed and presented in the work of Johari and Desabrais,[14] due to the FSIs of a parachute canopy during the terminal descent phase of deployment, the flexible canopy undergoes a "breathing" motion, in which the diameter at the skirt of the canopy oscillates about a mean value periodically.[1,18] Using a high-speed camera and image-processing routine,[19] the authors were able to extract the projected diameter of the canopy as a function of time. The root-mean-square amplitude of diameter fluctuations was found to be 3%–5% of the mean projected diameter, and the normalized breathing frequency (i.e., $f_b \cdot D_p/U_\infty$), or Strouhal number, was found to be nearly constant at 0.55. In order to determine the effect of canopy dynamics on drag and the development of the wake flow, a periodic motion was prescribed for the canopy using the data found from the experiment. The overall canopy shape was prescribed to undergo sinusoidal motion, where the base diameter, D_p, and depth, H, would oscillate 5% about the rigid canopy dimensions. While undergoing the periodic motion, the projected base diameter, D_p, would always be normal to the incoming free-stream flow. It was hypothesized that in order to conserve the length of the constructive diameter, D_0, the relationship between base diameter, D_p, and canopy depth, H, would be inversely proportional.

Using the free-stream velocity and projected diameter of the rigid canopy, the frequency of the oscillation, f_b, was calculated to be 1 Hz. The prescribed motion for the canopy base diameter and depth are illustrated in Fig. 4.

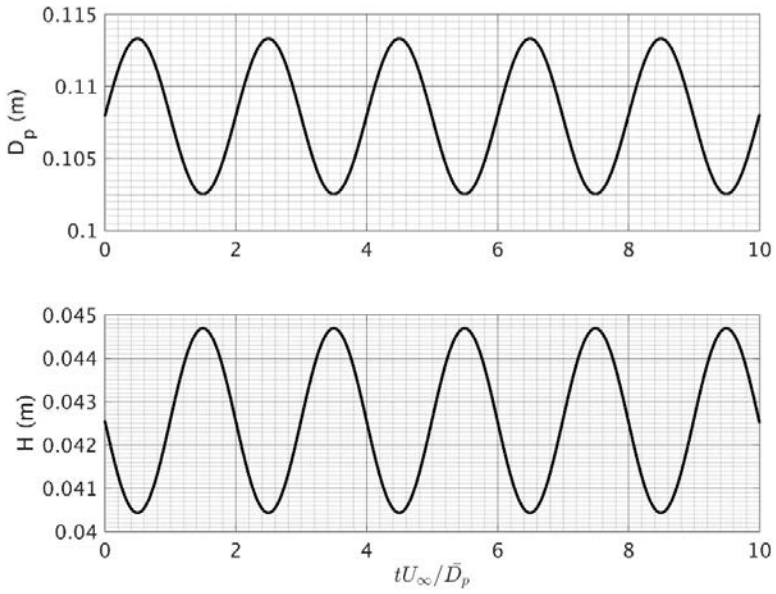

Fig. 4 Periodic oscillation prescribed for canopy base diameter (D_p) and depth (H)

A file-based mesh morphing motion was implemented to simulate the periodic oscillating canopy. This global mesh motion option interpolates the position and velocity of grid points by iteratively solving radial basis functions (RBF) at each time step. The velocity and acceleration of defined grid control points located on the boundary vertex nodes of the canopy were specified at five time-step intervals and then repeated until the end of the simulation. The five time steps correspond to the five equally spaced phase angles of a sinusoidal wave (i.e., ϕ = 0°, 90°, 180°, 270°, 360°). In order to reduce the computational load on the RBF interpolation algorithm, while also maintaining sufficient resolution of the canopy's surface, the total control points were reduced to 2211 boundary vertex nodes. Figure 5 presents the control points for the mesh morphing motion at the static (nominal) projected diameter, D_p, (x_0, y_0, z_0), maximum projected diameter (x_{max}, y_{max}, z_{max}) and minimum projected diameter (x_{min}, y_{min}, z_{min}) shapes. Furthermore, a mesh morphing region box was defined, to localize the morphing region around the canopy (i.e., 1 base diameter, D_p, from the center of the canopy hemisphere). The result of the mesh morphing on the computational domain at ϕ = 0°, 90°, 180°, 270°, and 360° is presented in Fig. 6. An animation of the mesh morphing is presented in Fig. 7.

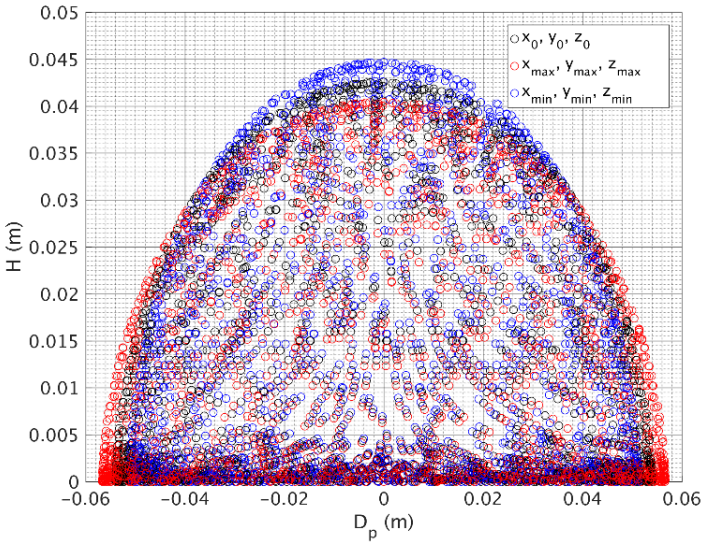

Fig. 5 Control points for mesh morphing at nominal (black), maximum (red), and minimum (blue) diameter shapes

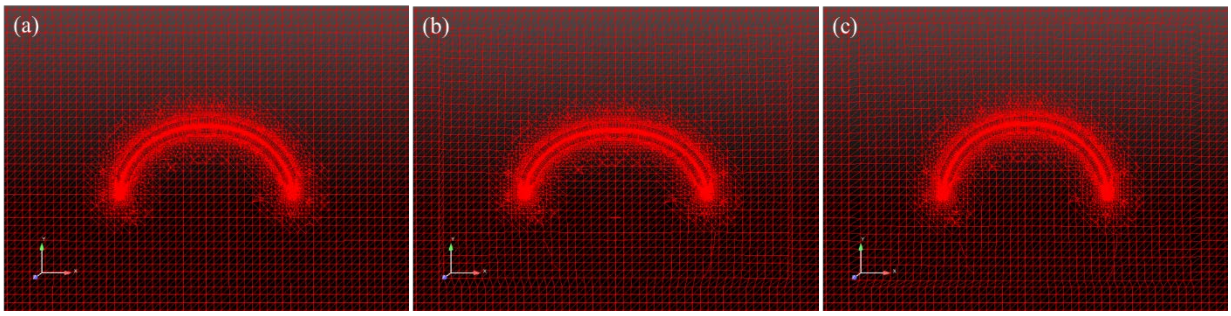

Fig. 6 Computational domain during mesh morphing at a) ϕ = 0°, 180°, 360°, b) ϕ = 90°, and c) ϕ = 270°

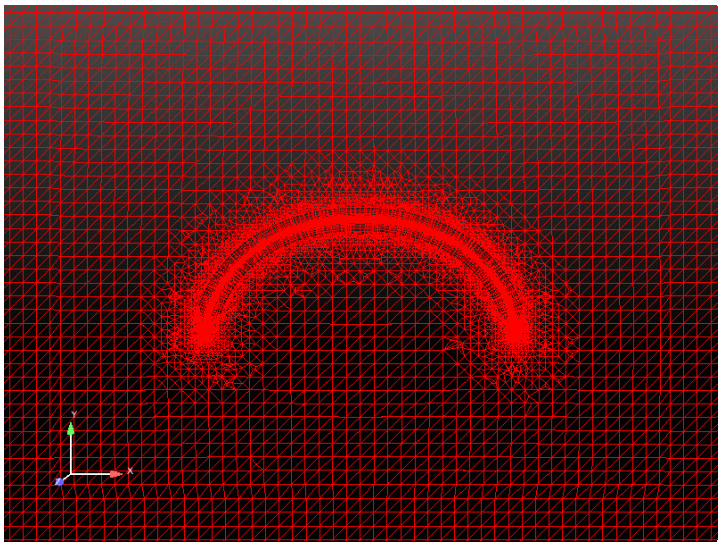

Fig. 7 Animation of computational domain during mesh morphing

2.2 Computational Fluid Dynamics (CFD) Solution Technique

The commercially available code, CFD++ v15.1.1, by Metacomp Technologies, Inc.[20] was used for all simulations. The 3-D incompressible preconditioned Reynolds-averaged Navier-Stokes (RANS) equations were numerically solved to compute the flow solution for each respective case. Steady-state and transient simulations were employed. Both unsteady RANS (URANS) and Hybrid RANS-LES models were studied. Specifically, the realizable k-ϵ (R k-ϵ) two-equation RANS turbulence model was used for all steady-state simulations, whereas, the cubic k-ϵ two-equation RANS turbulence model was used for URANS simulations. The Hybrid RANS-LES models studied were Metacomp's Batten-Goldberg Hybrid RANS-LES (LNS) model,[21] based on the cubic k-ϵ two-equation RANS turbulence model, and Improved Delayed Detached Eddy Simulation (IDDES) model,[22] based on the Spalart-Allmaras one-equation RANS turbulence model.[23]

All simulations were performed on the Cray XC40 supercomputers (GORDON, CONRAD) located at the US Navy DOD Supercomputing Resource Center (DSRC) at the Stennis Space Center, Mississippi.

For all steady-state simulations, the solution was advanced toward convergence using a point-implicit time integration scheme with local time-stepping, defined by the Courant-Friedrichs-Lewy (CFL) number. A linear ramping schedule was used to gradually increase the CFL number from 1 to 200 over the first 100 iterations after which the CFL remained constant until convergence was reached. The multigrid W-cycle method with a maximum of 4 cycles and a maximum of 20 grid levels were used to accelerate convergence. Implicit temporal smoothing was applied for the increased stability, which is especially useful where strong transients arise. The spatial discretization function was a second-order, upwind scheme using a Harten-Lax-van Leer-Contact Riemann solver and Metacomp's multi-dimensional Total-Variation-Diminishing flux limiter. Convergence for the total forces and moments was typically achieved in 1000 iterations, with residuals reducing at 6 orders or more in magnitude.

For all transient simulations, the dual-time step method was employed with the point-implicit time integration scheme, utilizing a global time step and an inner time step. The global time steps were selected based 100 steps per characteristic time (i.e., characteristic length, D_p, divided by free-stream velocity, U_∞, $\Delta t = 0.005$), with 15 inner iterations per global time step (the residuals reduced at least an order of magnitude in 15 inner steps). The number of global time steps were selected based on the Strouhal number (i.e., St $\approx$ 0.15) for a rigid hemispherical cup,[15,16] specifically, 10 cycles of the shedding frequency predicted, or approximately 30 s.

2.3 Flow Field and Boundary Conditions

All computations were completed using a free-stream temperature and pressure of 288.15 K and 101,325 Pa, respectively. The study was conducted with water as the selected fluid, at Re_{Dp} = 30,000, or a free-stream velocity of U_∞ = 0.22 m/s. The turbulence length-scale was calculated using values of free-stream turbulence intensity, T_u, and turbulent/laminar viscosity ratio, μ_T/μ, set to 3% and 50, respectively. The free-stream velocity, U_∞, and base diameter of the rigid canopy, D_p, were used to make the fluid flow variables and coordinates nondimensional, denoted by an asterisk, *. The domain was initialized using free-stream conditions everywhere. The inlet boundary condition was set as inflow, while the outlet condition was imposed using the predicted mass flow rate based on the incoming free-stream velocity and cross section of the water tunnel. The sidewalls of the water tunnel were modeled as inviscid, slip walls, as the experiment revealed negligible blockage effect, as well as negligible increased flow rate effect due to boundary layer growth on the walls. The surface of canopy was modeled as an adiabatic, no slip, viscous wall using the solve-to-wall methodology to model the boundary layer. The effect of permeability was simulated using equal wall bleeding and suction on the outer and inner surfaces of the canopy, respectively. The bleeding and suction rates were defined using a constant normal-to-wall mass flow rate based on a percentage of the incoming free-stream velocity and surface area of the exposed wetted surface of the hemisphere (i.e., $\pi \cdot D_p^2/2$).

3. Results and Discussion

The results obtained from the rigid canopy only investigation were studied first. The findings from the investigation were then used to determine which parameters to further pursue on both rigid canopy with forebody as well as for the periodic oscillating canopy investigation. The effect of turbulence model, free-stream turbulence level, permeability, upstream forebody wake, and canopy dynamics on drag and near wake flow field were investigated and compared to the experimental work on a flexible canopy.

3.1 Drag Prediction

3.1.1 Rigid Canopy Only

The drag coefficient, C_{Drigid}, of the rigid canopy was computed in CFD++ for all rigid configurations. The drag coefficient is calculated using Eq. 1.

$$C_{Drigid} = \frac{D}{\frac{1}{2}\rho_\infty U_\infty^2 S}, \quad (1)$$

where D is the drag force, ρ_∞ and U_∞ are the free-stream density and velocity, respectively, and S is the cross-sectional area of the canopy base (i.e., $S = \pi D_p^2/4$). The drag coefficient from the steady solution was calculated by computing the average drag force value from the last 200 iterative steps to smooth out some low-amplitude oscillations present. For the transient solutions, the time-averaged drag coefficient was computed using the last 300 global time steps.

The drag coefficient computed from each methodology is presented in Table 3. The wind tunnel–measured drag coefficient presented for reference was reported by Hoerner[24] based on sheet-metal "caps" as a function of their height ratio for Reynolds numbers between 10^4 and 10^6.

Table 3 Drag coefficient for a rigid canopy without the presence of a forebody

Case	$C_{Drigid,\infty}$
Wind tunnel (literature)	1.42
Steady CFD (realizable k-ϵ)	1.467
URANS (cubic k-ϵ)	1.416
Hybrid RANS-LES (LNS)	1.496
Hybrid RANS-LES (IDDES)	1.538

The predicted drag coefficient values from simulation match relatively well to literature on rigid hemispheres. The URANS solution implementing cubic k-ϵ turbulence model resulted in the lowest drag value, whereas both Hybrid RANS-LES models predict higher drag values, specifically, IDDES predicting approximately an 8% larger drag coefficient value than URANS. The Hybrid RANS-LES models are able to resolve vortical structures in the wake of the canopy. The results suggest that the flow structures in the wake cause a larger velocity deficit, and therefore, a larger drag coefficient value.

3.1.2 Rigid Canopy and Forebody

Previous investigations on parachutes have shown that the total drag can be reduced due to an upstream forebody.[25–27] Specifically, the wake generated from the forebody causes a region of decreased dynamic pressure upstream of the parachute, therefore reducing drag.[28,29] This deficit region reduces with higher parachute-to-forebody diameter ratios and with increased distance between forebody and parachute. An analytical method was developed by Peterson and Johnson[25] that predicts forebody wake effects from velocity distributions measured behind forebody configurations. The method uses empirical constants that are fitted to the wake velocity data at downstream locations of a forebody[28,29] (without a downstream parachute) to predict the ratio of parachute drag with the presence of a forebody (C_D) to that of a parachute without a forebody ($C_{D,\infty}$), and is presented in Eqs. 2–5.

$$\frac{C_D}{C_{D,\infty}} = 1 + \frac{2}{r_p^2} \cdot \frac{D_1}{D_2} \cdot \left[1 - e^{D_2 r_p^2} + \frac{D_1}{4} e^{2D_2 r_p^2} - \frac{D_1}{4}\right], \tag{2}$$

$$r_p = \frac{D_p}{D_{fb}}, \tag{3}$$

$$D_1 = \frac{a}{\left(Z/D_{fb}\right)^m}, \tag{4}$$

$$D_2 = \frac{-1}{0.435k^2\left(Z/D_{fb}\right)^{2n}}, \tag{5}$$

where r_p is the ratio of the projected base diameter of the parachute canopy to the diameter of the forebody, and Z is the streamwise canopy base diameter location downstream of the forebody. Here, the empirical constants, m, n, a, and k, are found by fitting the wake profile at a specified streamwise Z location with a velocity deficit profile given by Eq. 6. The empirical constants a and k are functions of the natural exponential of forebody drag coefficient (i.e., $a = C_1 \exp\left(C_2 \cdot C_{Dfb}\right)$), where C_1 and C_2 are constants.

$$\frac{U_\infty - u}{U_\infty} = \frac{a}{\left(Z/D_{fb}\right)^m} exp\left[\frac{-1}{0.435k^2\left(Z/D_{fb}\right)^{2n}}\right]. \tag{6}$$

Through the use of the described empirical method, the drag coefficient for the parachute canopy used in the experiment can be estimated. A steady-state CFD simulation using R k-ϵ turbulence model was performed for the forebody alone case. The drag coefficient of the forebody, C_{Dfb}, and wake velocity profile at a downstream distance L of the forebody (i.e., base canopy diameter location, z* = 0) was obtained.

For all simulations performed, the drag coefficient of the forebody was calculated using Eq. 7.

$$C_{Dfb} = \frac{Drag_{fb}}{\frac{1}{2}\rho_\infty U_\infty^2 S_{fb}} \tag{7}$$

where $Drag_{fb}$ is the drag force computed for the forebody and S_{fb} is the cross-sectional area of the forebody (i.e., $S_{fb} = \pi D_{fb}^2/4$). Using a parameter estimation routine (i.e., minimizing root mean square of error), the empirical constants that satisfy Eq. 6 for the wake velocity profile computed at a downstream location L from the forebody were found and are presented in Eqs. 7–10. The resulting wake velocity profile computed using the empirical constants were compared to the steady-state simulation results and is presented in Fig. 8.

$$m = 0.58 \tag{7}$$

$$n = 0.31 \tag{8}$$

$$a = 0.42\, exp\left(1.67 \cdot C_{Dfb}\right) \tag{9}$$

$$k = 0.2\, exp\left(1.22 \cdot C_{Dfb}\right). \tag{10}$$

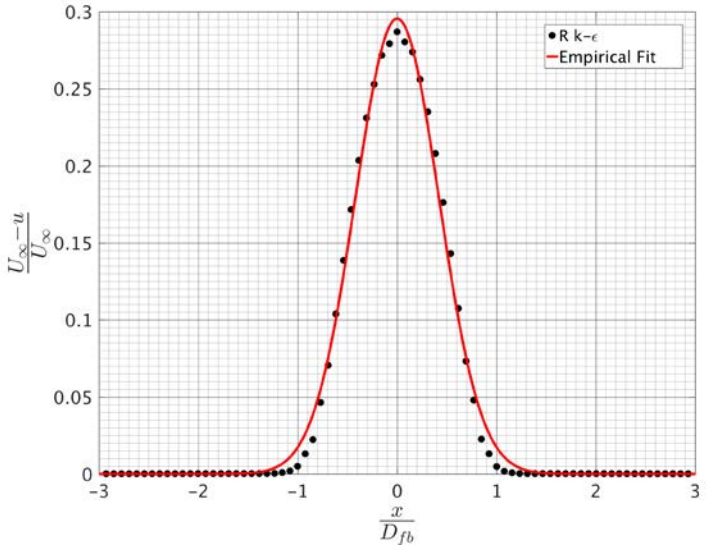

Fig. 8 Computed wake velocity profiles of forebody at z* = 0 ($z/D_{fb} \approx 11$) from steady-state simulation and empirical fit solution used in calculations

From the computed empirical constants, the estimated ratio of canopy drag in the presence of a forebody to that of a parachute without a forebody ($C_D/C_{D,\infty}$) was found using Eq. 2. Due to the large ratio of canopy diameter to forebody diameter, as well as a relatively small forebody wake width, the estimated ratio of canopy

drag with forebody to without a forebody was calculated to be approximately 0.98 (i.e., $C_D/C_{D,\infty} \approx 0.98$). Since the wake velocity profile and resulting empirical constants were found using R k-ϵ steady-state simulation, the drag coefficient of the rigid canopy without the presence of a forebody computed using the same methodology ($C_{Drigid,\infty} = 1.467$) was selected to estimate the drag coefficient of the rigid canopy with the presence of a forebody (C_{Drigid}).

Table 4 presents the estimated C_{Drigid} value obtained by using the empirical relation on the rigid canopy only simulation. In addition to the empirical prediction method, the rigid canopy and forebody were numerically simulated using the same methodologies as described previously. The computed drag coefficient of the rigid canopy with the presence of a forebody from each approach is presented in Table 4. Table 4 also shows the computed drag coefficient of the forebody with a canopy downstream.

Table 4 Drag coefficients for a rigid canopy with an upstream forebody

Case	C_{Drigid}	C_{Dfb}
Empirical ($C_D/C_{D,\infty} \approx 0.98$)	1.44	. . .
Steady CFD (R k-ϵ)	0.998	0.434
URANS (cubic k-ϵ)	0.978	0.385
Hybrid RANS-LES (LNS)	1.411	0.333
Hybrid RANS-LES (IDDES)	1.433	0.337

The empirical method predicted the drag coefficient of the parachute canopy with the presence of an upstream forebody to decrease approximately 2%. Similarly, both Hybrid RANS-LES turbulence models predict mild decreases of approximately 6% and 7%, respectively. The RANS simulations for both steady and transient simulations predict a substantial decrease in drag of approximately 31%. The large discrepancy in results are due to the difference between RANS and Hybrid RANS-LES turbulence models in resolving highly unsteady wake flow downstream of the canopy. The Hybrid RANS-LES models are able to accurately resolve the flow structures that are present in the near wake of the canopy, whereas the RANS models do not. Details of each respective computed flow field are discussed further in the following sections.

As previously discussed in detail, the drag of the canopy reduces due to the presence of an upstream forebody. Conversely, it is evident that the presence of a canopy downstream affects the wake flow and drag of the forebody. The computed drag coefficient of the forebody without a canopy downstream was found to be approximately 0.617 (i.e., $C_{Dfb} = 0.6173$). The drag coefficient of the forebody

decreases significantly due to the presence of the downstream canopy (Table 4). Furthermore, it is evident that the presence of a canopy downstream affects the wake flow of the forebody. The wake velocity profiles for all numerical techniques at two streamwise locations between the forebody and canopy, z* = –0.5 and –0.05, are presented in Figs. 9a and b, respectively.

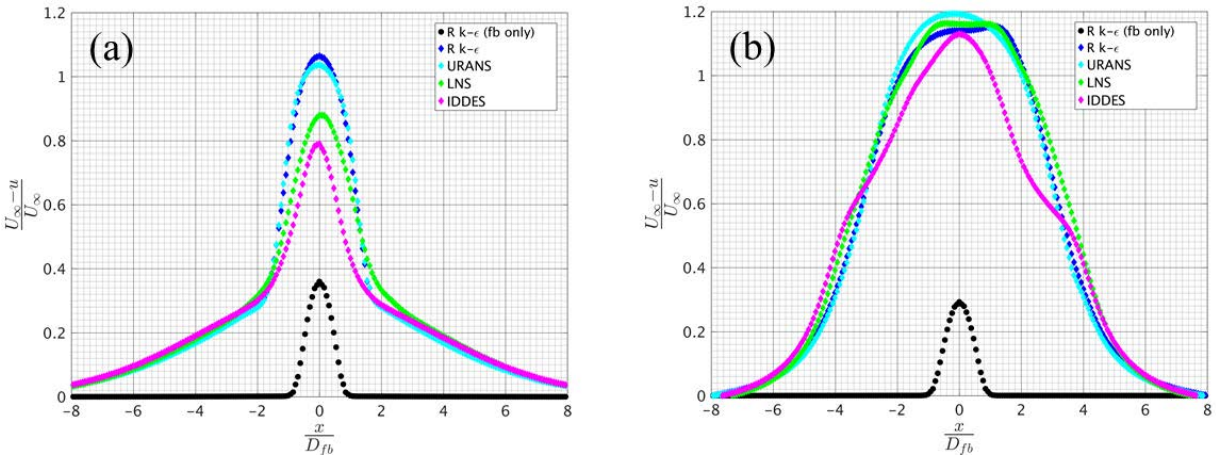

Fig. 9 Wake velocity profiles of forebody at a) z* = –0.5 ($z/D_{fb} \approx 7$) and b) z* = –0.05 ($z/D_{fb} \approx 10.5$) for forebody alone from steady simulation (black), forebody with the presence of a downstream canopy from steady simulation (blue), and time-averaged transient simulations using URANS (cyan), LNS (green), and IDDES (magenta) turbulence models

The wake velocity profile for the forebody with an upstream canopy is larger in width and magnitude compared to the forebody alone case. Moreover, the presence of the canopy seems to impose an overall offset to the velocity deficit, as the velocity profile asymptotically approaches to free-stream at a reduced rate compared to forebody alone configuration. The wake velocity profile computed using Hybrid RANS-LES turbulence models exhibit smaller deficit magnitude compared to both steady and unsteady RANS simulations. At the streamwise location close to the canopy base diameter, z* = –0.05, the effect of the canopy is more pronounced. All numerical simulations for the canopy with upstream forebody configuration produce a wake velocity profile that is considerably wider and larger in magnitude compared to the forebody alone configuration. Furthermore, the width of the deficit seems to extend to $x/D_{fb} \approx \pm 8$ in the cross-stream direction, which is the same length as the canopy base diameter (i.e., D_p). From Fig. 9b, it is evident that the deficit region just upstream of the canopy base diameter encompasses most of the incoming flow through the projected frontal area of the canopy.

The average drag coefficient for the flexible parachute with the same averaged geometric parameters, as measured by Johari and Desabrais[14] was found to be approximately 1 (i.e., $C_{Dflex} \approx 1$), similar to what was found for the RANS

simulation results when a forebody was modeled. Although the RANS simulation results compare better to the experiment, it is conjectured that the similarities are merely coincidental. Since the Hybrid RANS-LES models predict similar drag reduction as calculated by the well-established empirical method and better resolve the highly unsteady wake flow of the rigid canopy, the results from the Hybrid RANS-LES simulations are presumed to be more accurate for this specific investigation (i.e., rigid canopy with forebody). These discrepancies suggest that the rigid canopy is not a suitable model for a flexible canopy. Moreover, the results validate that coupled FSI simulation techniques are necessary to accurately predict drag. The flexible canopy is able to deform due to FSI, which can cause large fluctuations in aerodynamic properties of the canopy. Furthermore, as noted in the experiment, the flexible canopy exhibited a periodic "breathing" motion, which would affect the development of the wake. Another factor to consider is the permeability of the fabric of the canopy. These types of behaviors can help explain the large discrepancies in drag between rigid and flexible canopies and are discussed in the following sections.

3.1.3 Periodic Oscillating Canopy

The next parameter explored was the effect of canopy dynamics. A periodic oscillating motion, in which both base diameter, D_p, and depth, H, was prescribed as a function of time for the rigid canopy. Both the base diameter and canopy depth periodically oscillated at 10% peak to peak about the mean values that were used in the rigid canopy simulations (D_p and H).

The drag coefficient, C_{Dpo}, of the periodic oscillating canopy was computed in CFD++ at each global time step of simulation. The drag coefficient for the periodic oscillating canopy as a function of time is calculated similarly to Eq. 1 and is presented in Eq. 11.

$$C_{Dpo}(t) = \frac{D(t)}{\frac{1}{2}\rho_\infty U_\infty^2 S}, \tag{11}$$

where $D(t)$ is the drag force as each global time step, and S is the cross-sectional area of the canopy base of the mean projected base diameter, or the diameter used in the rigid canopy study (i.e., $S = \pi\bar{D}_p^2/4$). The instantaneous drag coefficient of both the rigid canopy and periodic oscillating canopy with and without the presence of an upstream forebody for the last 20 s (i.e., 4000 global time steps) for URANS, LNS, and IDDES turbulence models compared to the flexible canopy from the experiment is presented in Figs. 10a and b, respectively.

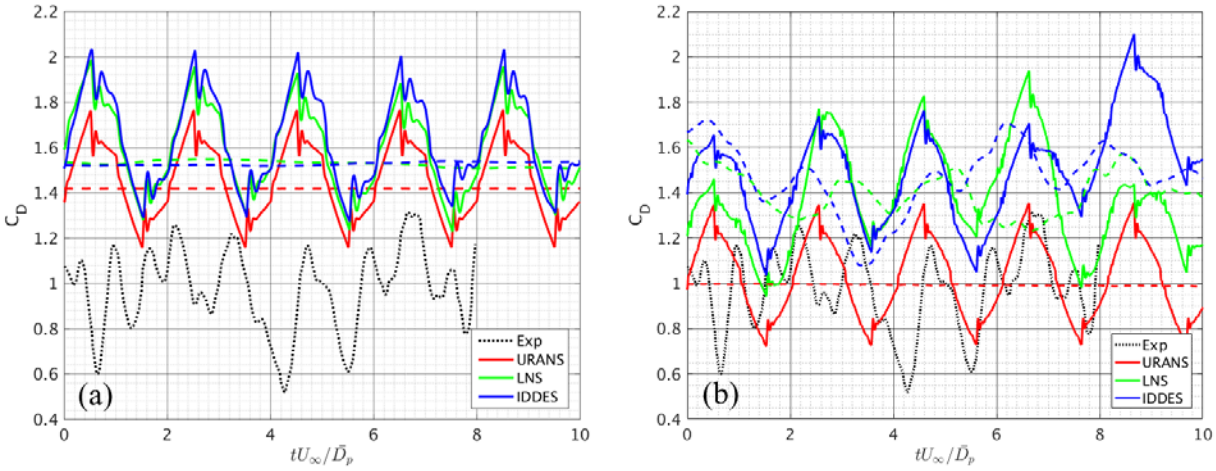

Fig. 10 Instantaneous drag coefficient for a flexible parachute (Exp), for a rigid canopy (dashed line), and for a periodic oscillating canopy (solid line) a) without and b) with an upstream forebody, using URANS (red), LNS (green), and IDDES (blue) turbulence models

Compared to the rigid canopy (dashed line), the periodic oscillating canopy shows large fluctuations in drag. The drag is periodic and directly coupled to the motion prescribed to the canopy. Conversely, although the drag from the experiment is unsteady, it is not coupled to the motion of the canopy. The authors from the experiment found that the power spectral measurement of the signal did not result to a large peak at the "breathing" frequency. Furthermore, as was found previously for the rigid canopy case, the predicted drag for the periodic oscillating canopy is larger compared the flexible canopy from the experiment. These large discrepancies found in simulation can be attributed to differences in canopy motion and the resulting canopy shape. In the experiment, the flexible canopy shape is directly defined from the FSI, and that change in profile of the canopy is not strictly linear. Additionally, the flexible canopy is attached by tethers, and is able to move freely in all directions. Whereas, the simulation performed has a prescribed motion at a fixed position, in which the concavity of the canopy is preserved.

Although the predicted drag from the periodic oscillating canopy does not match well to the experiment, several features and trends can be identified and discussed when comparing the selected turbulence models. All turbulence models produce a drag history signal that is not purely sinusoidal. Furthermore, the peaks of the signal show disturbances that are at a higher frequency. The results suggest that there may be vortical flow structures that are being produced and shed when the canopy experiences zero velocity motion, which causes fluctuations in drag.

The URANS model produces a drag coefficient that oscillates about the rigid canopy drag value. Interestingly, the Hybrid RANS-LES turbulence models produce drag values that are on average larger than their corresponding rigid

canopy case. One explanation for the larger drag values could be that the Hybrid RANS-LES models are resolving the additional vortical flow structures that are generated near the skirt of the canopy as the canopy oscillates. The additional flow structures alter the size and structure of the wake, and may produce a larger velocity deficit. The Hybrid RANS-LES models reveal that there is a dynamic effect present for the periodic oscillating canopy that causes an increase in drag.

The presence of the forebody also induces unsteadiness in the drag coefficient value for both rigid RANS-LES cases and periodic oscillating canopy cases (Fig. 10b). Unlike the URANS model, the Hybrid RANS-LES models are able to resolve the flow structures that are generated by the forebody, which causes the unsteadiness in drag coefficient for both rigid and periodic oscillating canopy cases. Compared to the canopy alone case, it is conjectured that the unsteadiness present for the canopy and forebody configuration is due to characteristic frequencies associated to a combination of the shedding, mixing layer, and recirculating regions of the forebody wake. These results help explain some of the unsteadiness in the drag coefficient signal observed in the experiment. Moreover, as was previously discussed, there is an overall reduction in drag of the canopy due to the forebody.

3.2 Time-Averaged Flow Field Data

The flow field data from both steady and time-averaged data were computed after convergence was achieved. The time-averaged data for the transient simulations were collected 0.5 s after initiating the unsteady simulation from the steady solution, sampling every time step until the physical time reached 30 s (6000 time steps). Data analysis was performed on each flow field, for each respective configuration. The time-averaged flow field data for the rigid canopy with and without upstream forebody are first compared and discussed, followed by a discussion on the effect of a periodic oscillating canopy on the near wake flow field.

3.2.1 Rigid Canopy

As discussed, the wake of the forebody causes a reduction in the drag for an upstream canopy. The wake alters the flow field entering the canopy, specifically reducing the dynamic pressure upstream of the canopy. To help observe this flow phenomena, the nondimensional pressure coefficient, C_P, was computed (Eq. 12) in CFD++ for all configurations with and without the presence of a forebody.

$$C_P = \frac{p - p_\infty}{\frac{1}{2}\rho_\infty U_\infty^2}, \tag{12}$$

where p is the static pressure at the current point being evaluated. The pressure coefficient from the steady solution was calculated by computing the average value from the last 200 iterative steps. For the transient solutions, the time-averaged pressure coefficient was computed using the last 300 global time steps.

Figure 11 show contours of nondimensional pressure on a horizontal slice (y* = 0) through the canopy obtained from steady RANS (a, e), URANS (b, f), LNS (c, g), and IDDES (d, h) flow solutions for both rigid canopy alone (a–d) and with upstream forebody (e–h) configurations. The contour slice was taken from each respective flow solution, along the centerline of the canopy, beginning at 2 canopy diameters upstream from the canopy, z* = –2, to 2 diameters downstream, or z* = 2. The forebody spans from approximately 3 to 1.4 canopy diameters upstream of the base diameter of the canopy, or z* = –3 to –1.4, and has a diameter that is approximately 0.13 canopy diameters, spanning from x* = –0.065 to x* = 0.065. For all configurations, there are regions of higher pressure present inside of the canopy and lower pressure regions downstream in the wake of the canopy. The Hybrid RANS-LES models predict larger magnitudes for both high- and low-pressure regions compared to the RANS-based models for both configurations. For the canopy only configurations, the Hybrid RAN-LES models exhibit a larger deficit region in both span and streamwise directions compared to the RANS-based models (c–d). Upstream of the canopy, the regions of higher pressure also extend farther upstream, indicating that the canopy causes a back pressure influence.

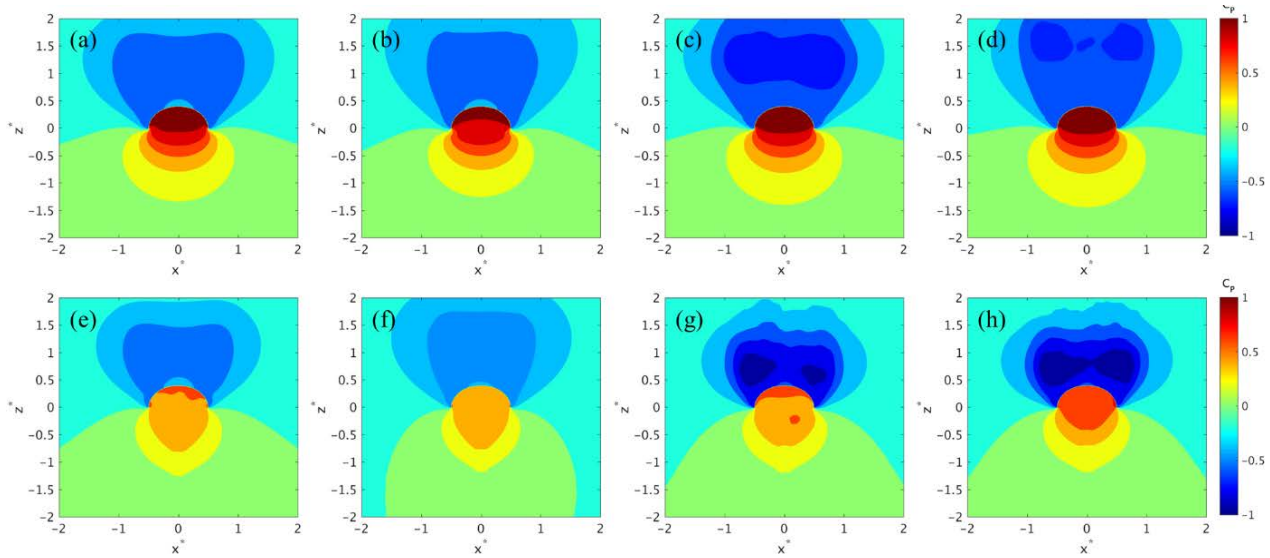

Fig. 11 Contours of pressure coefficient at y* = 0 for rigid canopy only (a–d) and rigid canopy with upstream forebody (e–h), computed from steady RANS (a, e), URANS (b, f), LNS (c, g), and IDDES (d, h)

The influence of an upstream forebody causes an overall reduction in high-pressure regions inside the canopy (e–h). The RANS-based models show a greater magnitude decrease compared to the Hybrid RANS-LES models. The back pressure generated by the canopy extends approximately 1.5 canopy diameters upstream, which imposes higher pressure aft of the forebody. The pressure difference across the forebody decreases, therefore reducing the overall pressure drag of the forebody. Interestingly, the behavior of the low-pressure regions in the wake trend differently between RANS-based models and the Hybrid RANS-LES models. The magnitude of pressure decreases significantly for the Hybrid RANS-LES models compared to the RANS models. Furthermore, the forebody causes an increase in concentration of low pressure closer to the surface of the canopy for the Hybrid RANS-LES models (g–h), whereas the RANS models show little to no effect.

Contours of nondimensional streamwise velocity at $y^* = 0$, or centerline, from steady RANS (a, e), URANS (b, f), LNS (c, g), and IDDES (d, h) flow solutions for both rigid canopy alone (a–d) and with upstream forebody (e–h) configurations are presented in Fig. 12. The contour slice was taken from each respective flow solution, along the centerline of the canopy, beginning a quarter of a diameter upstream from the canopy, $z^* = –0.25$, to 5 diameters downstream, or $z^* = 5$. All simulation cases show similar wake flow structure, with regions of recirculating flow in the near wake of the rigid canopy. The streamwise velocity contours show the reverse flow region downstream of the canopy, indicative by regions of negative velocity values. Similarly to the steady RANS solution, all time-averaged solutions show an approximate symmetry of the primary wake flow structure. As expected, the wake flow region for the steady RANS case matches best with the URANS flow solution. The Hybrid RANS-LES cases show a smaller deficit region compared to the RANS-based solutions. The higher-fidelity turbulence model flow solutions show that the negative velocity region extends approximately 2 diameters downstream from the base of the canopy, whereas both RANS solutions predict a wake that is more streamlined, extending to approximately 3 diameters downstream.

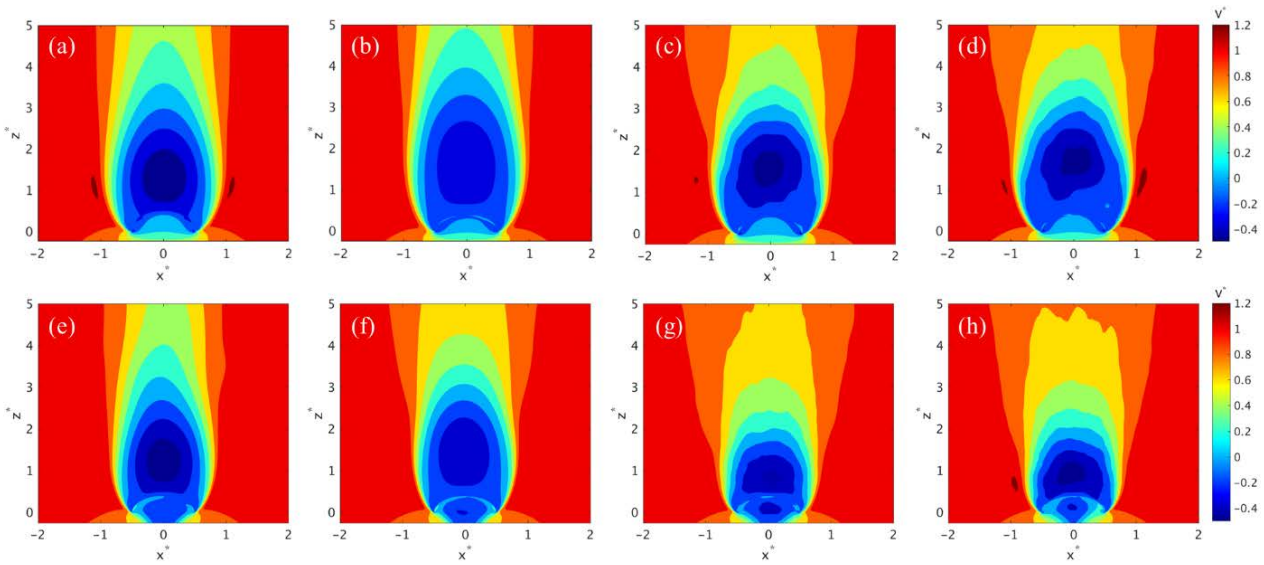

Fig. 12 Contours of nondimensional streamwise velocity at y* = 0 for rigid canopy only (a–d) and rigid canopy with upstream forebody (e–h), computed from steady RANS (a, e), URANS (b, f), LNS (c, g), and IDDES (d, h)

The upstream forebody causes an overall reduction in wake width for all configurations. Furthermore, there is an increase in velocity magnitude present inside of the canopy. The forebody causes flow to enter the canopy, which causes a reduction in pressure as observed in Fig. 11. The Hybrid RANS-LES cases show a significantly smaller deficit region residing near the canopy surface (g–h). Moreover, the wake extends approximately 1.6 canopy diameters downstream, which is similar to the wake shape observed for a flexible parachute from water tunnel experiment.

Contours of nondimensional out-of-plane vorticity at y* = 0, or centerline, from steady RANS (a, e), URANS (b, f), LNS (c, g), and IDDES (d, h) flow solutions for both rigid canopy alone (a–d) and with upstream forebody (e–h) configurations are presented in Fig. 13. The contour slice was taken from each respective flow solution, along the centerline of the canopy, beginning a quarter of a diameter upstream from the canopy, z* = –0.25, to 5 diameters downstream, or z* = 5. The out-of-plane vorticity contours for each case show the formation of symmetric vorticity regions about the canopy. For both RANS solutions, these vorticity regions extend farther and remain coherent farther downstream than the Hybrid RANS-LES solutions. The Hybrid RANS-LES solutions are able to show the unsteadiness of the flow by resolving the secondary flow structures in the wake near the surface of the canopy. The presence of the forebody causes flow structures to enter the canopy for all configurations, indicated by regions of positive and negative vorticity regions. The forebody directs flow into the canopy, causing regions of recirculation. In the wake, the shape and size of the vortical structures

are altered as well. For all configurations, the magnitude of the vorticity is reduced, and seems to remain coherent farther downstream compared to the canopy-only cases. Furthermore, the concentrations of vorticity are significantly smaller and closer to the canopy surface for the Hybrid RANS-LES models due to the increased turbulent mixing that can be predicted using these models. Overall, the forebody seems to induce more flow structures in the wake.

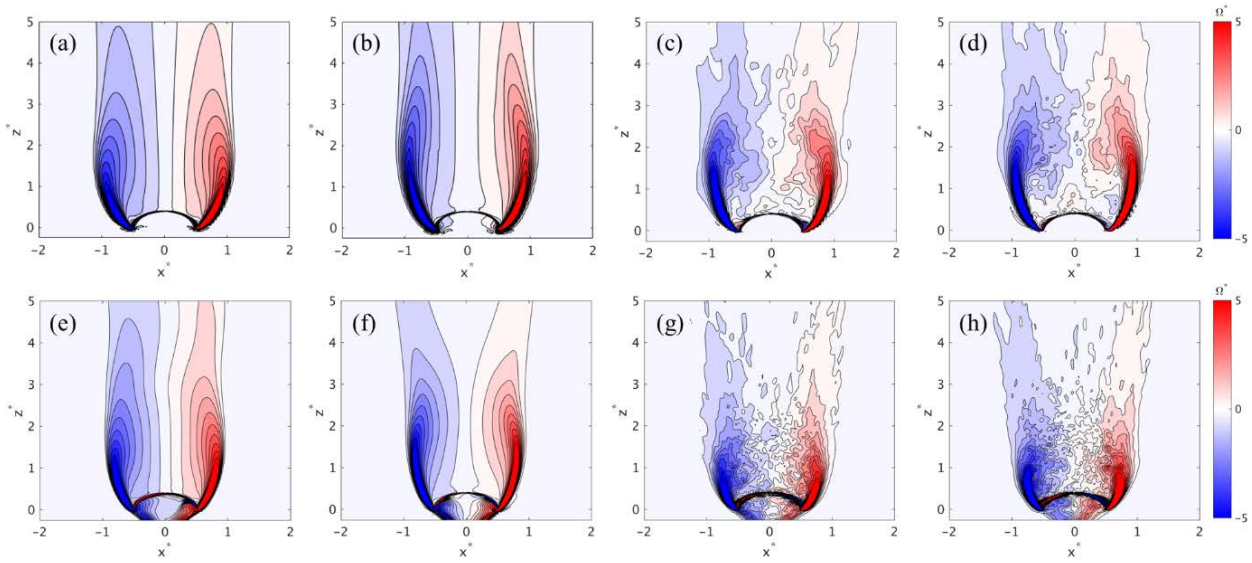

Fig. 13 Contours of nondimensional out-of-plane vorticity at y* = 0 for rigid canopy only (a–d) and rigid canopy with upstream forebody (e–h), computed from steady realizable k-ϵ (a, e), URANS (b, f), LNS (c, g), and IDDES (d, h)

Streamlines on the same horizontal slice from steady RANS (a, e), URANS (b, f), LNS (c, g), and IDDES (d, h) flow solutions for both rigid canopy alone (a–d) and with upstream forebody (e–h) configurations are presented in Fig. 14. The streamline velocity field for all turbulence models is qualitatively similar. A large flow structure causes the flow to recirculate, with reverse flow present along the centerline of wake downstream of the canopy. The streamlines show that for all simulations, the recirculating regions are relatively symmetric. The RANS-LES turbulence models show that the recirculating region remains closer to the surface, whereas the RANS turbulence models show the extension of the wake region stretch farther downstream. The streamlines are closer together in the recirculating region for the higher fidelity turbulence models, indicating that the magnitude of the velocity in the regions is stronger compared to both RANS models. The presence of the forebody causes the wake region to reduce in streamwise length and remain closer to the surface (e–h). The recirculating regions for the Hybrid RANS-LES models are significantly reduced; however, the magnitude of the velocity increases. These results compare well to the observed streamlines from the water tunnel experiment.

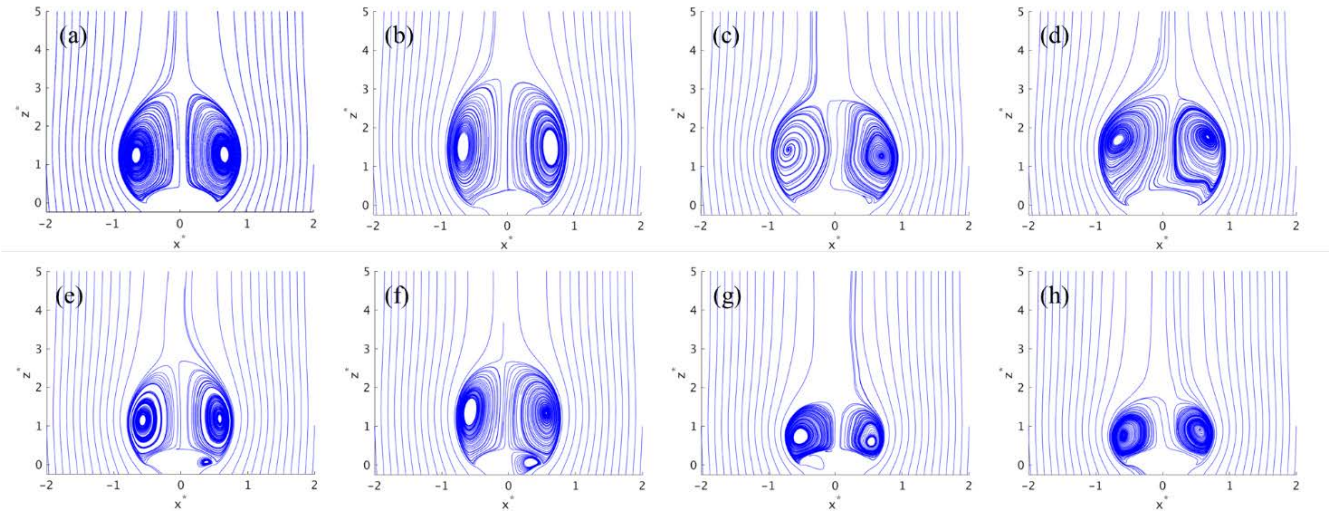

Fig. 14 Contours of streamwise streamlines at y* = 0 for rigid canopy only (a–d) and rigid canopy with upstream forebody (e–h), computed from RANS (a, e), URANS (b, f), LNS (c, g), and IDDES (d, h)

In addition to qualitative contour plots, quantitative data can be explored. Line plots of nondimensional streamwise velocity (a–d), out-of-plane vorticity (e–h), and Q-criterion (i–l) at z* = 0.25, 0.5, 1, 1.5, 2, and 3 for rigid canopy only and with the presence of an upstream forebody computed from steady RANS (a, e, i), URANS (b, f, j), LNS (c, g, k), and IDDES (d, h, l) are presented in Figs. 15 and 16, respectively. The cross-stream distributions for all parameters are relatively symmetric and qualitatively similar in shape. The velocity profiles downstream of the rigid canopy show the magnitude and extent of the velocity deficit in the wake. As was observed in the Fig. 14, the wake extends farther downstream for both RANS turbulence models compared to the RANS-LES models. Furthermore, the vorticity profiles show larger magnitude in peak of vorticity for the RANS-LES turbulence models. Moreover, as was found in the contour plots, secondary flow structures are present near the surface of the canopy for the RANS-LES turbulence models, which are indicated by unsteady vorticity values along the span within the wake region. The Q-criterion was computed and investigated in order to define vortical structures in the wake by identifying regions where the vorticity tensor dominates the rate of strain. The RANS-LES turbulence models show larger peak values in Q-criterion, indicating that the structures are stronger compared to the RANS models.

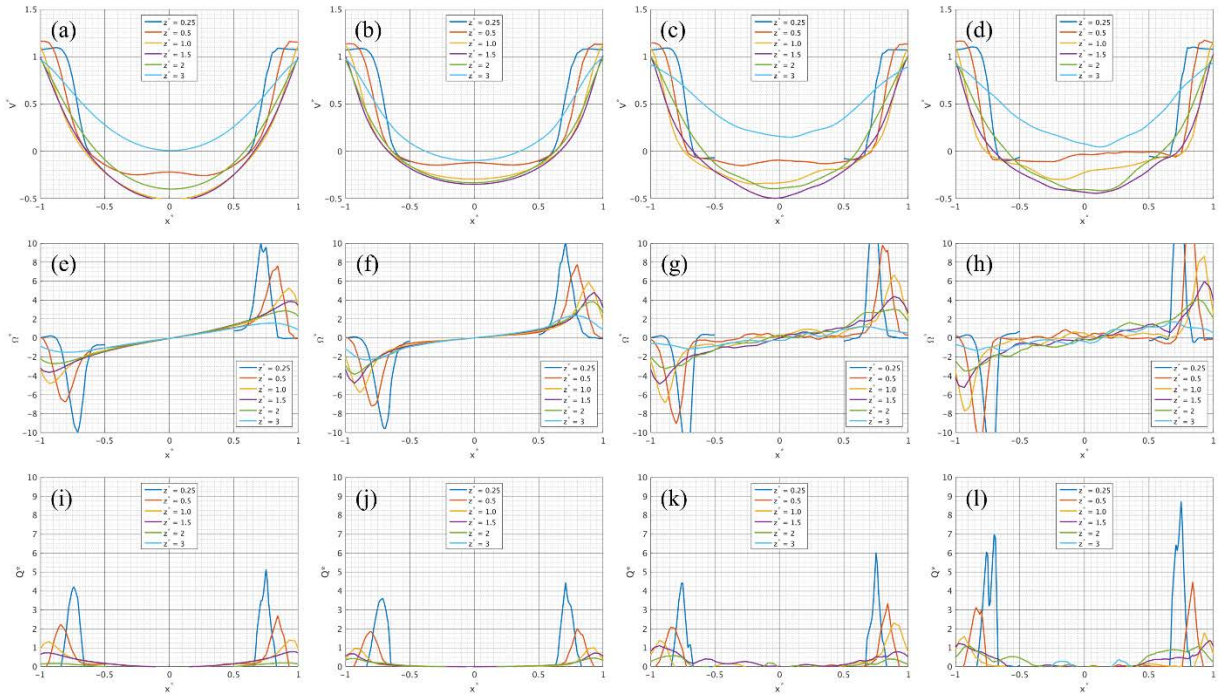

Fig. 15 Line plots of nondimensional streamwise velocity (a–d), out-of-plane vorticity (e–h), and Q-criterion (i–l) at z* = 0.25, 0.5, 1, 1.5, 2, and 3 for steady RANS (a, e, i), URANS (b, f, j), LNS (c, g, k), and IDDES (d, h, l) (rigid canopy only)

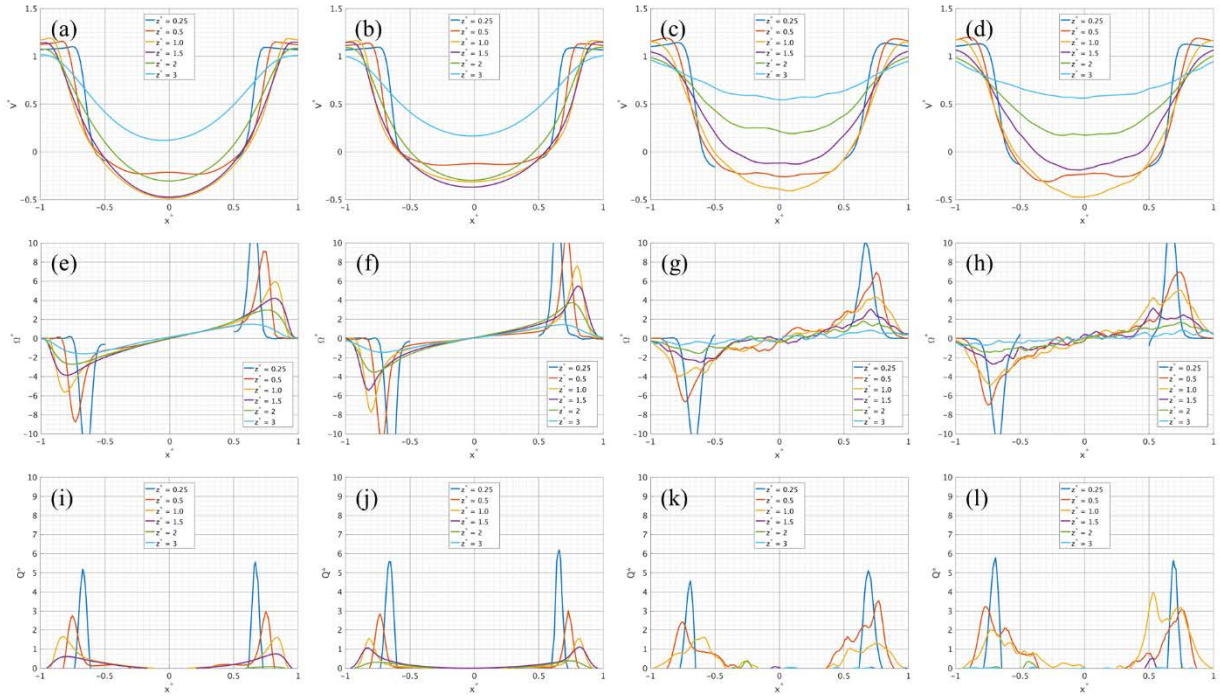

Fig. 16 Line plots of nondimensional streamwise velocity (a–d), out-of-plane vorticity (e–h), and Q-criterion (i–l) at z* = 0.25, 0.5, 1, 1.5, 2, 3 for steady realizable k-ϵ (a, e, i), URANS (b, f, j), LNS (c, g, k), and IDDES (d, h, l) (rigid canopy with forebody)

As was found previously, the presence of the upstream forebody affects the wake characteristics of the canopy (Fig. 16). Compared to the rigid canopy only case, the wake deficit region recovers sooner downstream. This effect is more noticeable for the Hybrid RANS-LES flow field solution, as the velocity deficit returns to a positive value at between 1.5 and 2 diameters downstream of the canopy, whereas the same occurred at 3 diameters for the canopy alone configuration. Furthermore, as was found in the contour plots, the width of velocity deficit region decreases. Interestingly, an inverse relationship is observed for vorticity between RANS and Hybrid RANS-LES flow solutions. Whereas the peak vorticity values seem to increase for the RANS solution with a presence of a forebody, the overall magnitude vorticity values for the Hybrid RANS-LES solution decreases for the same configuration. This behavior is also observed for the Q-criterion values.

In addition to spanwise velocity profiles within the wake, the axial velocity, or the streamwise velocity along centerline as a function of downrange distance from the canopy surface for both without and with an upstream forebody configurations are presented in Figs. 17a and b, respectively. The surface of the canopy is at $z^* \approx 0.4$. The centerline velocity profile is able to quantify the velocity deficit region within the wake and able to show the decay and growth of velocity. Similarly observed from the previous figures, the URANS solution matches the steady RANS solution best downstream, whereas the Hybrid RANS-LES models match well with each other. The differences between each respective turbulence model (i.e., RANS and Hybrid RANS-LES, respectively) are evident near the surface of the canopy downstream. Farther downstream, each respective turbulence model seems to converge. As was found earlier, the velocity deficit region for the RANS models extends farther downstream and recovers to a lower velocity value than for the RANS-LES turbulence models.

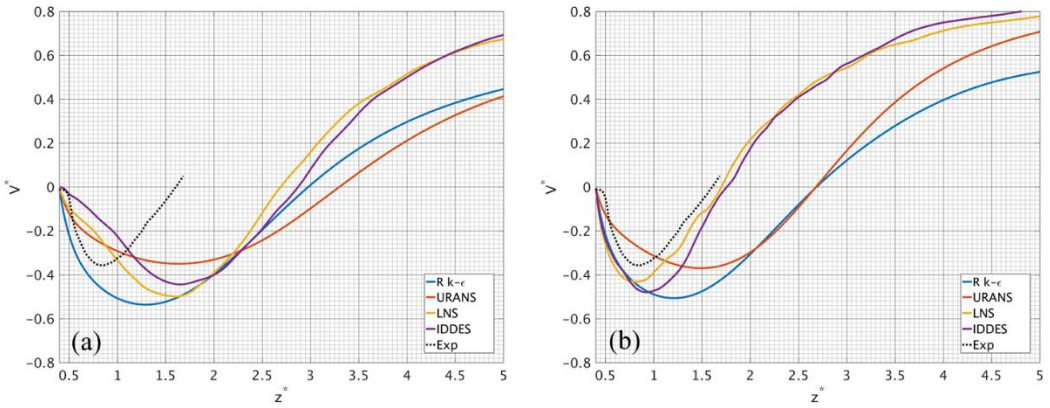

Fig. 17 Nondimensional streamwise velocity at x* = 0 as a function of downstream distance for a flexible canopy (Exp), and for a rigid canopy a) without and b)with the presence of an upstream forebody, using realizable k-ϵ (blue), URANS (orange), LNS (yellow), and IDDES (purple) turbulence models

The effect of the forebody is most noticeable for the Hybrid RANS-LES simulations than for the RANS simulations. The RANS-LES turbulence models are able to qualitatively match the shape of the velocity profile of the experimental data. The near wake computed from RANS simulations shows little difference between configurations (i.e., with and without forebody); however, the URANS models indicate a velocity recovery sooner downstream. The LNS turbulence model matches best to the experiment, as the magnitude of the velocity deficit is closest to the experiment. The difference in velocity magnitude helps explain the overprediction of drag coefficient for the rigid canopy. Both Hybrid RANS-LES models seem to converge downstream to a higher velocity value sooner downstream compared to the canopy only configuration. These results reinforce the importance of modeling all geometries or payloads present upstream of the canopy. In conclusion, the wake flow of the canopy is altered due to the presence of an upstream forebody.

The experimental data presented are from the water tunnel experiments for a flexible canopy. Although the simulations do not match perfectly to the experiment, modeling the upstream geometry as well as using Hybrid RANS-LES models can be used to qualitatively predict the wake flow features of a flexible canopy. The results suggest that the differences between experiment and simulation may be due to a combination of canopy dynamics (i.e., FSI) and permeability.

3.2.2 Periodic Oscillating Canopy

As previously discussed, the rigid canopy was unable to accurately predict the drag and near wake flow field for a flexible canopy. Therefore, canopy dynamics was identified as a parameter necessary to model in order to accurately predict drag and wake flow features. Ideally, a fully coupled FSI code would be implemented to determine the natural dynamics of the canopy; however, a beneficial first step in the interim is to simply impose a dynamic motion on the canopy to determine and understand the potential effect of canopy dynamics on both drag and near wake flow. As discussed, the authors from the experimental work were able to obtain the projected diameter of the flexible canopy as a function of time. Using these results, a periodic oscillating motion, in which both base diameter, D_p, and depth, H, was prescribed as a function of time for the rigid canopy. Both the base diameter and canopy depth periodically oscillated at 10% peak to peak about the mean values that were used in the rigid canopy simulations (D_p and H).

To improve our understanding of the effect of the turbulence model on the development of the wake, time-averaged flow field data for the periodic oscillating canopy were analyzed. Contours of nondimensional streamwise velocity (a–c), out-of-plane vorticity (d–f), and streamwise streamlines (g–i) at $y^* = 0$, or centerline

for the periodic oscillating canopy from URANS (a, d, g), LNS (b, e, h), and IDDES (c, f, i) flow solutions, for both without and with the presence of an upstream forebody are presented in Figs. 18 and 19, respectively.

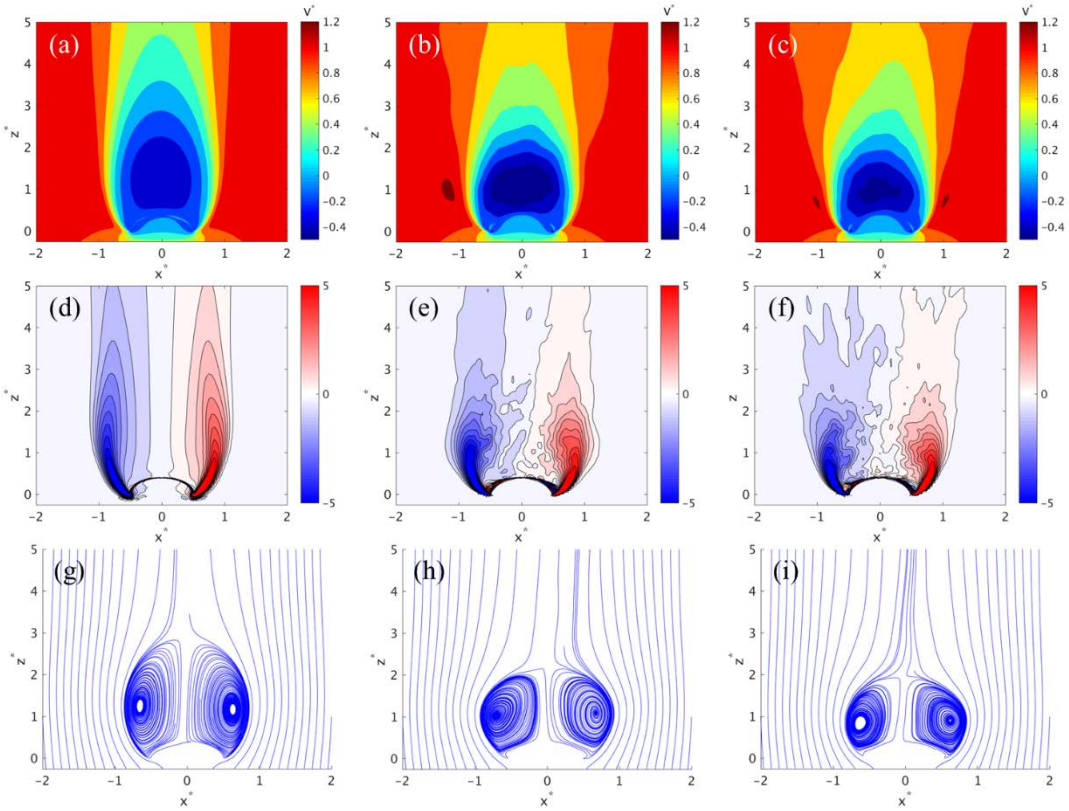

Fig. 18 Contours of nondimensional streamwise velocity (a–c), out-of-plane vorticity (d–f), and streamwise streamlines (g–i) at y* = 0, for rigid canopy only, using URANS (a, d, g), LNS (b, e, h), and IDDES (c, f, i) turbulence models (periodic oscillating canopy)

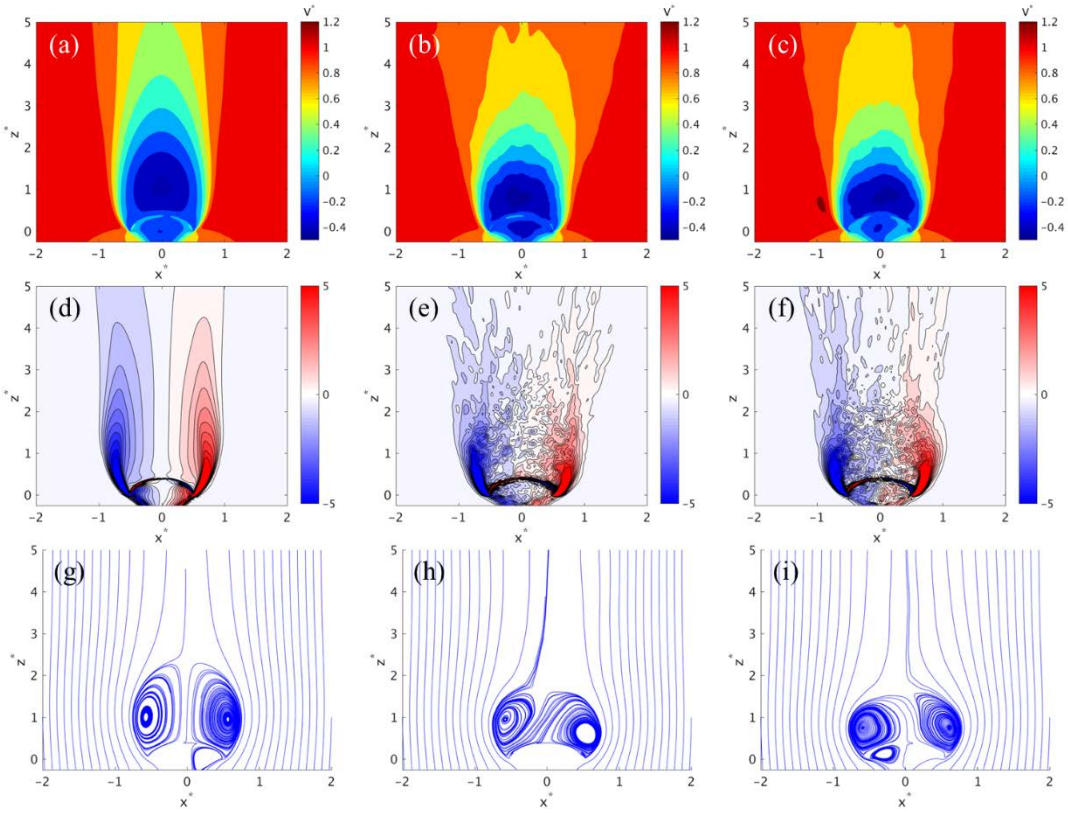

Fig. 19 Contours of nondimensional streamwise velocity (a–c), out-of-plane vorticity (d–f), and streamwise streamlines (g–i) at y* = 0, for rigid canopy with forebody present, using URANS (a, d, g), LNS (b, e, h), and IDDES (c, f, i) turbulence models (periodic oscillating canopy)

The streamwise velocity contours are able to show the size and structure of the near wake flow of the canopy. Similarly to the rigid case, all models show an approximate symmetric flow field with regions of negative velocity in the near wake. The URANS solution for the periodic oscillating canopy produces a near identical flow field to that of the rigid canopy case. The results support the earlier finding, in which the mean drag predicted using URANS on the periodic oscillating canopy matched the drag value predicted for the rigid canopy. Conversely, the Hybrid RANS-LES flow solution shows a substantially smaller wake than compared to their corresponding rigid canopy case. The height of the wake is reduced to approximately two canopy lengths; however, the magnitude of negative velocity near the canopy surface increased. The IDDES model produced the smallest wake, with also a smaller region of negative velocity in the center of the near wake.

Similarly to the rigid canopy case, the out-of-plane vorticity contours for all models show symmetric vorticity regions about the canopy. As discussed, the time-averaged URANS flow solution produced a flow field almost identical to its rigid

canopy case. The Hybrid RANS-LES solutions show a reduction in downstream extent of vorticity compared to the rigid canopy case. Furthermore, as similarly seen for the rigid canopy cases, the Hybrid RANS-LES models are able to show the presence of secondary flow structures in the center of the wake, as well as near the surface of the canopy.

The velocity streamline field for the Hybrid RANS-LES turbulence models shows smaller regions of recirculation. The centers of each recirculating region are closer to the canopy surface than compared to the rigid canopy case. Moreover, the streamlines are closer together, indicating that the velocity magnitude in wake is increased. The effect of canopy dynamics is less noticeable for the canopy with forebody configuration. Both streamwise velocity contours and streamlines show slight differences in wake height and width. However, the vorticity contours computed using Hybrid RANS-LES turbulence models again indicate additional flow structures present in the wake. These results suggest that additional vortical flow structures are being generated in the near wake of the canopy due to oscillation.

Line plots of nondimensional streamwise velocity (a–d), out-of-plane vorticity (e–h), and Q-criterion (i–l) at $z^* = 0.25$, 0.5, 1, 1.5, 2, and 3 for periodic oscillating canopy only and with the presence of an upstream forebody computed from RANS (a, e, i), URANS (b, f, j), LNS (c, g, k), and IDDES (d, h, l) are presented in Figs. 20 and 21, respectively. Similarly found in the previous figures, the canopy dynamics are able to alter the development of the wake flow. Compared to the rigid canopy alone configuration, the introduction of the periodic oscillation motion causes the wake to reduce in size, as the velocity deficit at downstream locations of $z^* = 2$ and 3 seem to recover sooner than for the rigid equivalent configuration. Similarly found in Fig. 18, the Hybrid RANS-LES models show a decrease in the height of the wake; however, the magnitude of the velocity deficit increases in the near wake of the canopy. For both vorticity and Q-criterion distributions, the magnitude for each parameter reduces compared to the rigid canopy configurations.

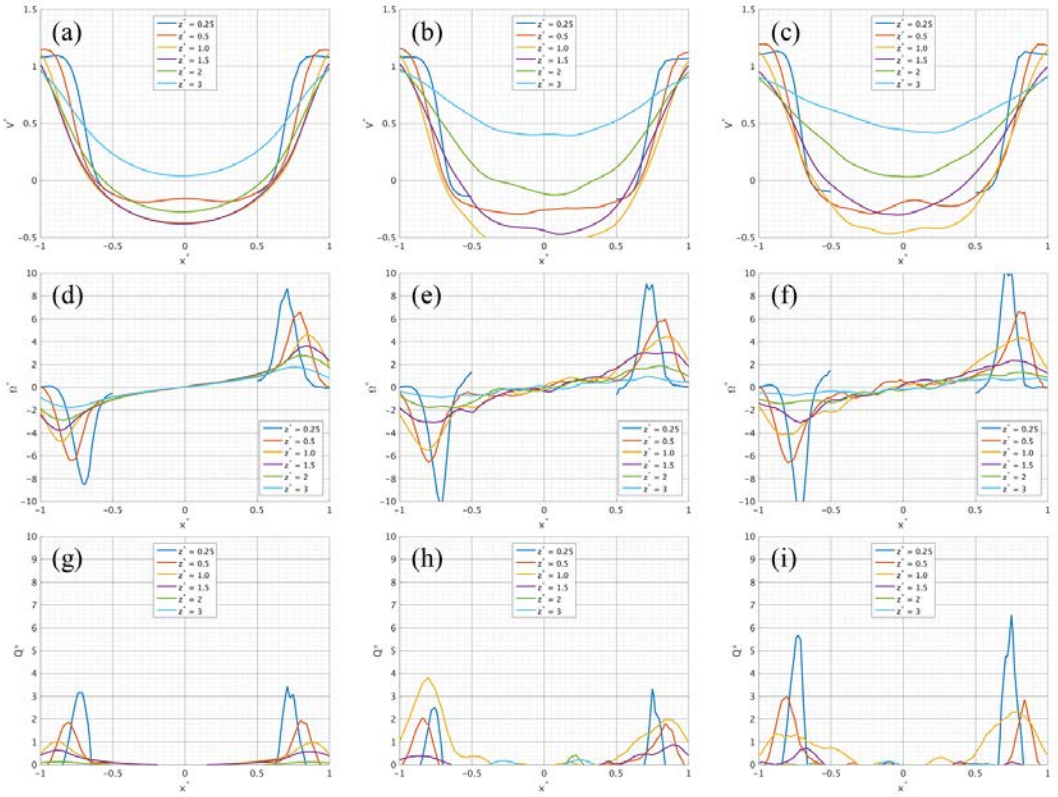

Fig. 20 Line plots of nondimensional streamwise velocity (a–c), out-of-plane vorticity (d–f), and Q-criterion (g–i) at z* = 0.25, 0.5, 1, 1.5, 2, and 3 for URANS (a, d, g), LNS (b, e, h), and IDDES (c, f, i) (periodic oscillating canopy without forebody)

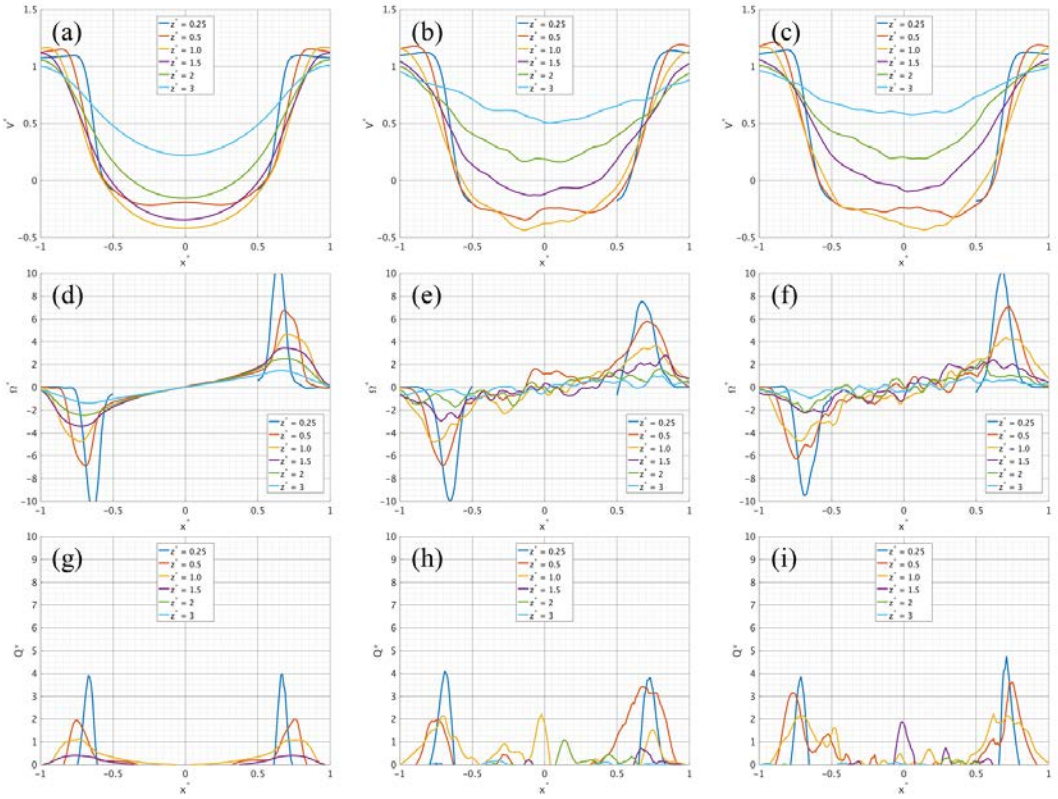

Fig. 21 Line plots of nondimensional streamwise velocity (a–c), out-of-plane vorticity (d–f), and Q-criterion (g–i) at z* = 0.25, 0.5, 1, 1.5, 2, and 3 for URANS (a, d, g), LNS (b, e, h), and IDDES (c, f, i) (periodic oscillating canopy with forebody)

As was found previously, the effect of canopy dynamics is less noticeable for the canopy with an upstream forebody configuration. For all parameters discussed, the magnitudes within the wake seem to be independent of canopy motion. However, the influence of the canopy motion can be observed in the unsteadiness present in the flow. The distributions of all discussed parameters are noisier compared to the rigid cases and are most evident in the flow solutions computed using Hybrid RANS-LES turbulence models.

In order to obtain quantifiable information on the near wake of the periodic oscillating canopy, line plots of time-averaged velocity deficit were again analyzed. The nondimensional streamwise velocity along centerline as a function of downrange distance from the canopy surface for a flexible canopy (experiment), rigid canopy (dashed), and periodic oscillating canopy (solid) for both without and with forebody is presented in Figs. 22a and 22b, respectively. As similarly observed previously, the dynamic effect of canopy motion results in a reduction in height of the velocity deficit region. The velocity deficit recovers sooner downstream than compared to the rigid canopy cases. With the addition of canopy dynamics, the velocity deficit behind a periodic oscillating canopy using Hybrid RANS-LES

turbulence models matched best to the flexible canopy from the experiment. Moreover, both Hybrid RANS-LES turbulence models converge to a similar velocity deficit profile. The results indicate that the combination of canopy dynamics and influence of an upstream geometry have the largest effect in determining the size and shape of the near wake of a parachute canopy. The difference in prescribed motion versus the actual motion the canopy undergoes can help explain the differences between simulation and experiment. It is hypothesized that if a higher fidelity, more accurate motion were prescribed for the canopy, the results would match better. Therefore, the current study reinforces the importance of performing coupled fluid dynamics-structural dynamics simulations to accurately model the motion and shape of parachute canopies.

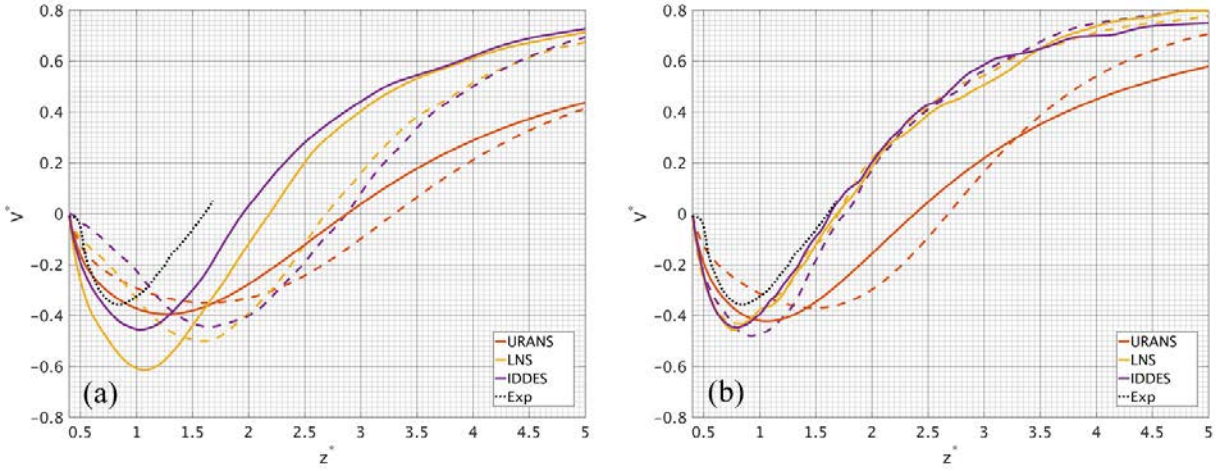

Fig. 22 Nondimensional streamwise velocity at x* = 0 as a function of downstream distance for a flexible canopy (Exp), a rigid canopy (dashed), and for a periodic oscillating canopy (solid), a) without and b) with an upstream forebody, using URANS (orange), LNS (yellow), and IDDES (purple) turbulence models

3.3 Instantaneous Flow Data

3.3.1 Rigid Canopy

In addition to the time-averaged data, instantaneous data from the transient simulations were analyzed. Figure 23 presents the iso-surface of nondimensional Q-criterion at Q* = 7.5, for both rigid canopy alone (a–c) and with an upstream forebody (d–f) using URANS (a, d), LNS (b, e), and IDDES (c, f) turbulence models at an instantaneous time at 30 s from the start of the transient simulations. The Q-criterion was used to show the development of flow structures that are present in the wake for each turbulence model. The single Q-criterion value, Q* = 7.5, was chosen in order to best identify flow structures in the wake. Similarly to what was found previously, the URANS solution was unable to resolve the flow

structures that are shed in the wake. The Hybrid RANS-LES turbulence models were studied in order to resolve the wake eddies in the flow. Both Hybrid RANS-LES models show the presence of secondary flow structures in the wake. The number of flow structures in the wake increases with the presence of an upstream forebody. Additionally, the vortical structures are smaller, and remain coherent farther downstream. As previously found and discussed, the RANS simulations shows little to no change in the flow structures that are present with the introduction of a forebody. Compared to the canopy alone configuration, there are significantly more structures near the canopy surface, both inside and outside of the canopy, and the width of the wake is overall reduced. Moreover, the Hybrid RANS-LES models are able to resolve vortical flow structures that are generated aft of the forebody that enters the canopy.

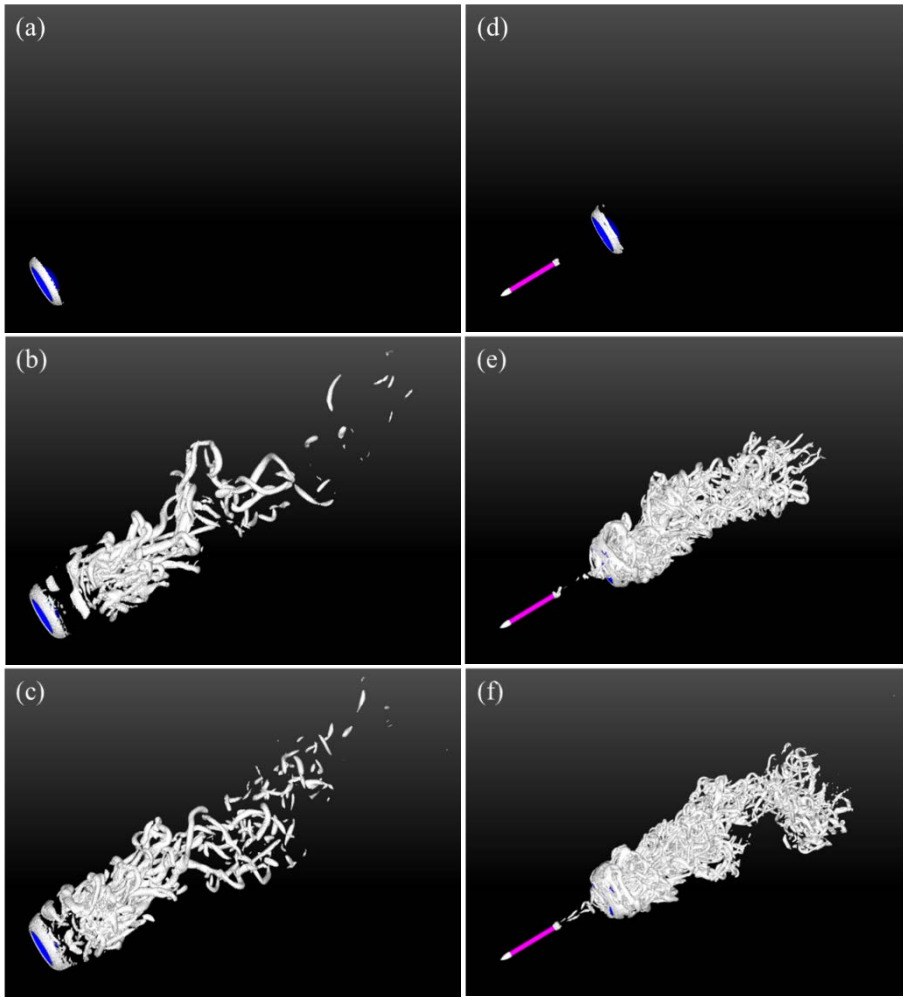

Fig. 23 Iso-surface of nondimensional Q-criterion at Q* = 7.5, for both rigid canopy without forebody (a–c) and with an upstream forebody (d–f) using URANS (a), LNS (b), and IDDES (c) turbulence models at an instantaneous time at 30 s from the start of the transient simulations

3.3.2 Periodic Oscillating Canopy

In addition to the time-averaged data, instantaneous data at phase angles, $\phi = 0°$, 90°, 180°, 270°, and 360°, of the periodic oscillating motion from the transient simulations were analyzed. Figures 24 and 25 present iso-surfaces of nondimensional Q-criterion at $Q^* = 7.5$, for both rigid canopy alone (Fig. 24) and with an upstream forebody (Fig. 25) using URANS (a–e), LNS (f–j), and IDDES (k–o) turbulence models at phase angles, $\phi = 0°$ (a, f, k), 90° (b, g, l), 180° (c, h, m), 270° (d, i, n), and 360° (e, j, o), from the last second of the transient simulations (i.e., t = 29 s, 29.25 s, 29.5 s, 29.75 s, and 30 s, respectively). Similarly to Fig. 23, the single Q-criterion value, $Q^* = 7.5$, was chosen in order to best identify flow structures in the wake. The URANS solution shows the formation and shedding of a coherent vortex ring that is directly coupled to the frequency of the prescribed periodic canopy motion (Figs. 24a–e). The vortex ring initially forms at the skirt of the canopy (Fig. 24a). The vortex ring then grows in size as the diameter of the canopy increases, until reaching a maximum when the diameter of the canopy reaches a maximum (Fig. 24b). The vortex ring then begins to lift off the surface of the canopy as the diameter of the canopy reduces, until it finally sheds from the surface (Fig. 24c). The vortex ring then advects downstream, increasing in size, while reducing in strength, until the vortex ring no longer remains coherent (Figs. 24d–c). As was found for the rigid canopy case, both Hybrid RANS-LES models show the presence of secondary flow structures in the wake (Figs. 23b–c and 24f–o, respectively). Compared to the rigid canopy case, there are more flow structures present near the surface of the canopy, as well as farther downstream in the wake. Although the secondary flow structures within the wake seem to be uncoupled to the prescribed motion, the global size and shape of the wake seem to be affected by the periodic oscillating motion. Specifically, there are more coherent flow structures near the skirt of the canopy, which seems to be coupled to the prescribed frequency (Figs. 24f–o). The flow solutions from the Hybrid RANS-LES turbulence models are able to show global effects in wake size and structure when the canopy is undergoing a periodic motion.

Similar findings are present for the canopy with forebody configuration. The URANS simulations only show a formation of a vortex ring that advects downstream, which loses coherence soon downstream. The generation of the vortex ring is coupled to the imposed oscillation. The Hybrid RANS-LES models show that there are more, although smaller, flow structures present in the wake. The periodic oscillation motion seems to have the largest noticeable effect in the shape of the wake. Specifically, the width of the wake may be coupled to the imposed oscillation motion.

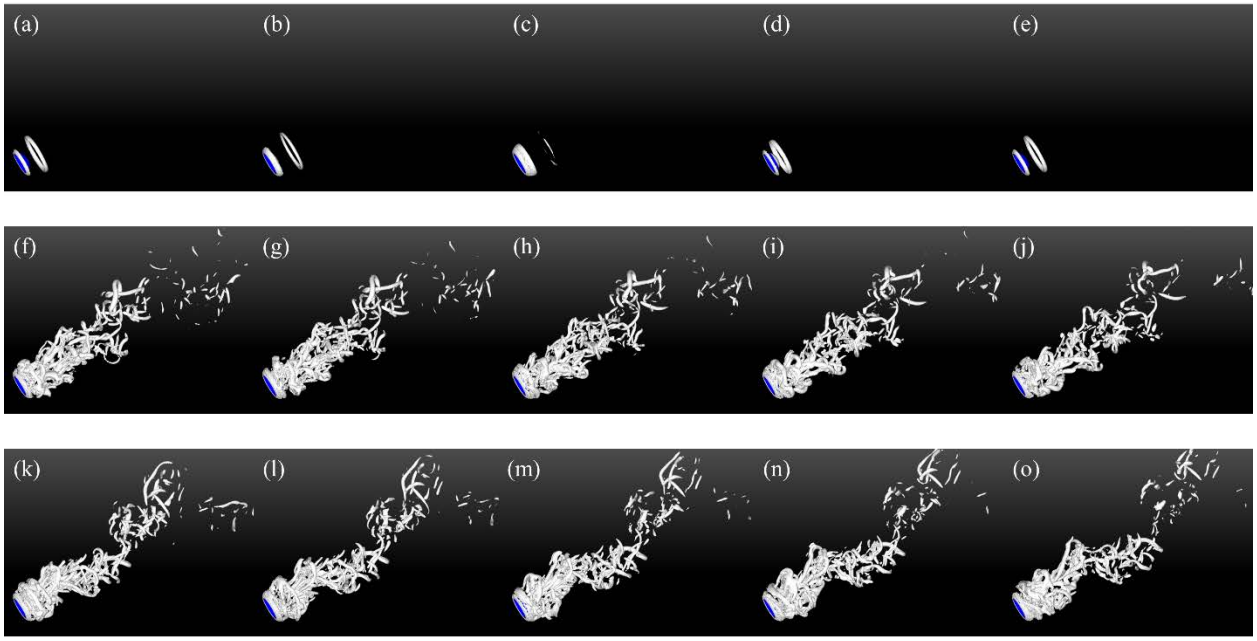

Fig. 24 Iso-surface of nondimensional Q-criterion at Q* = 7.5, for rigid canopy without forebody using URANS (a–e), LNS (f–j), and IDDES (k–o) at phase angles, ϕ = 0° (a, f, k), 90° (b, g, l), 180° (c, h, m), 270° (d, i, n), and 360° (e, j, o) from the last second of the transient simulations (i.e., t = 29, 29.25, 29.5, 29.75, and 30 s, respectively)

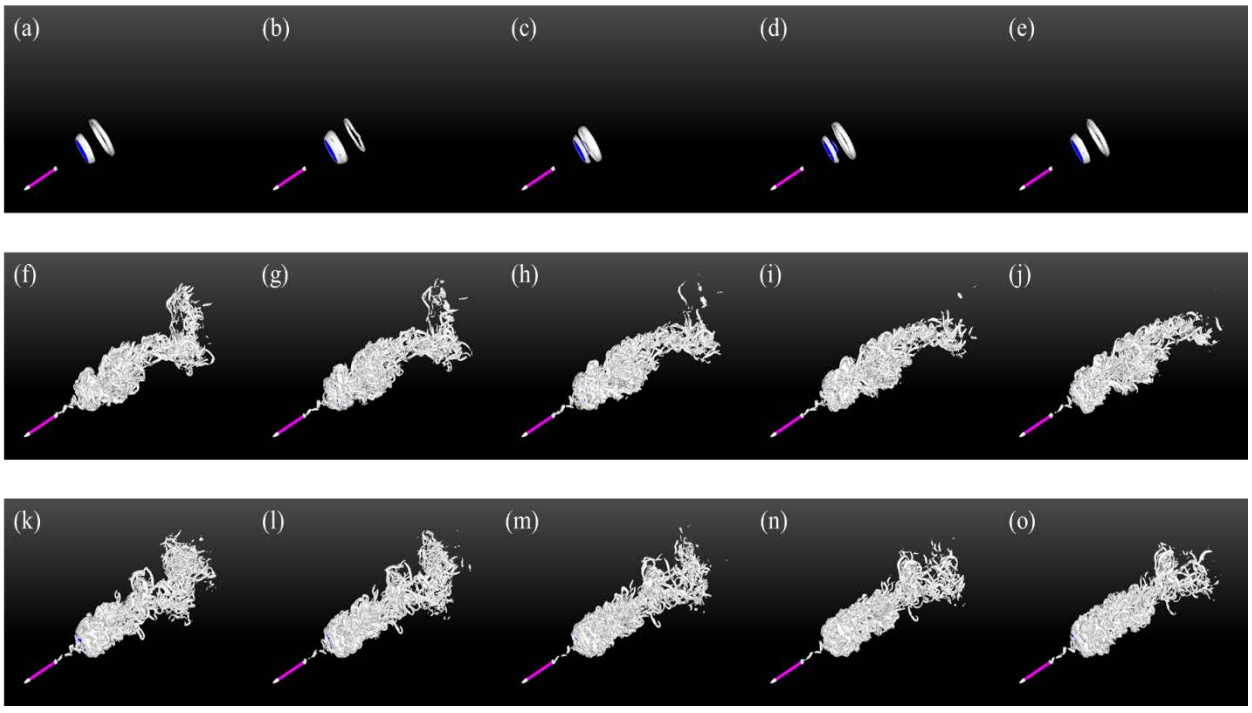

Fig. 25 Iso-surface of nondimensional Q-criterion at Q* = 7.5, for rigid canopy with forebody using URANS (a–e), LNS (f–j), and IDDES (k–o) at phase angles, ϕ = 0° (a, f, k), 90° (b, g, l), 180° (c, h, m), 270° (d, i, n), and 360° (e, j, o) from the last second of the transient simulations (i.e., t = 29, 29.25, 29.5, 29.75, and 30 s, respectively).

3.4 Vortex Shedding Frequency Characterization

The wake flow of the canopy contains numerous highly unsteady vortical flow structures that eventually shed downstream. The next investigation performed was to study the vortex shedding characteristics in the near wake of both rigid and periodic oscillating canopies. The authors from the experimental work on the flexible canopy revealed that the spectral analysis of the wake revealed prominent frequency peaks at both $St = 0.55$ (corresponding to the breathing frequency of the canopy) as well as $St = 0.16$, which is similar to both $St \approx 0.15$ and $St \approx 0.14$ that are associated with frequencies from wake flows of rigid cups and circular flat disks in the same Reynolds-number range, respectively.[16,30,31] The same authors also performed a separate study that characterized shedding frequencies in the near wake of rigid axisymmetric bluff bodies, specifically both smooth and ridged (to model gores of flexible canopy) rigid canopies with similar dimensions used in both previous water tunnel experiment and this computational investigation.[16] Similar to hot-wire anemometry used in the experiment,[16] in this study velocity probes were placed in the computational domain to measure the velocity fluctuations in the wake. The velocity probes were positioned to measure the instantaneous streamwise velocity at each transient simulation time step (i.e., 0.005 s). A total of 2000 samples were collected and analyzed.

The shedding characteristics were measured at the edge of the wake at specific downstream and spanwise locations listed in Table 5. The edge of the wake locations were determined based on the approximate spanwise (x*) location of peak vorticity at each streamwise (z*) position for the Hybrid RANS-LES turbulence models as presented in Figs. 15 (g–h) and 16 (g–h). For reference, the positions of the hot-wire probe selected from the experiment (i.e., rigid canopy) are presented in Table 5.

Table 5 Streamwise and spanwise measurement locations

z*	x* (canopy only)	x* (canopy with forebody)	x* (rigid canopy from experiment)
0.25	0.71	0.66	0.69
0.5	0.8	0.73	. . .
1.0	0.91	0.82	0.81
1.5	0.96	0.82	0.81
2	0.96	0.75	. . .
3	0.96	0.75	0.75

As previously discussed, the presence of an upstream forebody reduces the width of the wake. For each given downstream location, the width of the wake for the canopy with forebody configuration is significantly smaller, from approximately 10% in the near wake to greater than 20% farther downstream. This reduction in width explains the observed reduction in the predicted drag values. Furthermore, the profile of the wake for the rigid canopy with forebody as computed in simulation matches quite well to the experiment. The hot-wire probe locations from the experiment for the rigid canopy configurations are less than 5% to what was predicted in simulation. The similarity in wake profiles indicate that the Hybrid RANS-LES models are able to accurately predict wake size as well as suggest that the resulting computed drag for the rigid canopy with forebody configuration are close to the actual values.

The instantaneous nondimensional streamwise velocity measured by the probes from simulation for rigid canopy alone (a, d, g), rigid canopy with forebody (b, e, h), and periodic oscillating canopy with forebody (c, f, i), using URANS (a–c), LNS (d–f), and IDDES (g–i) turbulence models is presented in Fig. 26. For each given configuration, the Hybrid RANS-LES models exhibit larger fluctuations in velocity compared to the URANS turbulence model, as they are able to resolve more flow structures in the wake. The Hybrid RANS-LES models predict similar fluctuating velocity magnitudes for each configuration as well. The introduction of an upstream forebody (b, e, h) causes an increase in velocity fluctuations. The wake of the forebody upstream of the canopy causes unsteadiness in the wake flow of the canopy. The periodic oscillating canopy motion is observed in the velocity measurements farther downstream for the URANS model (c); however, it is less noticeable for the Hybrid RANS-LES models. As was observed in Fig. 25, it is hard to discriminate the flow structures that were generated due to canopy motion for the Hybrid RANS-LES models.

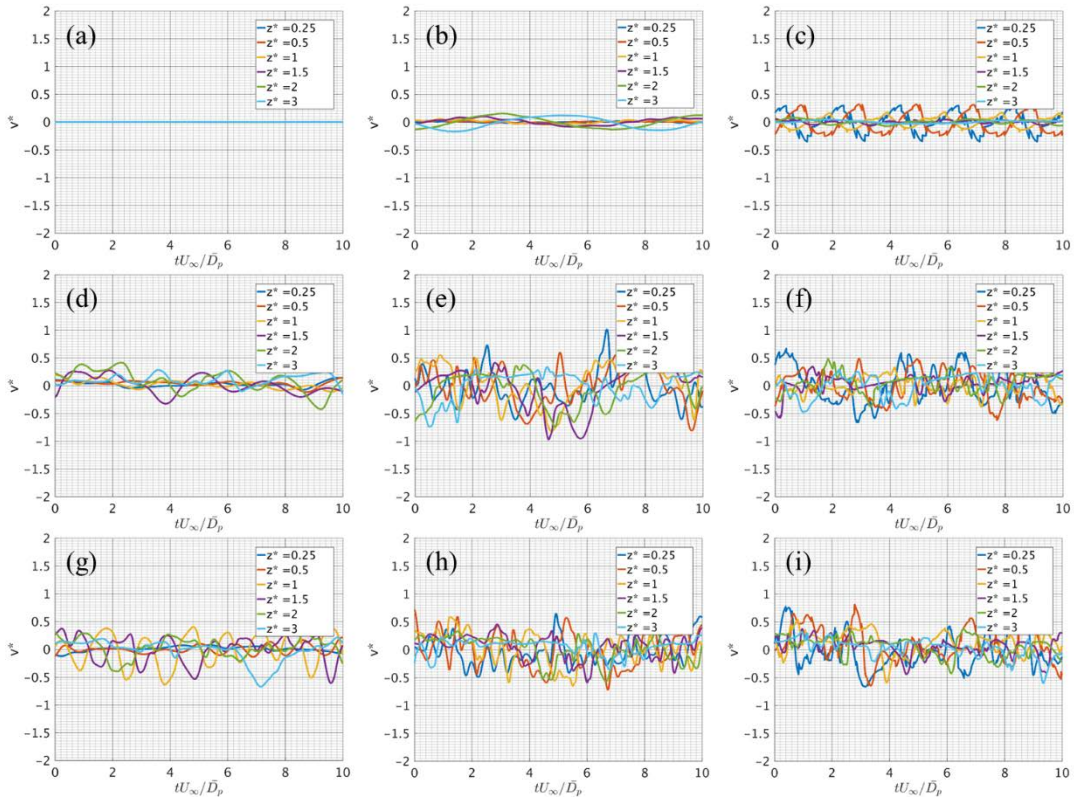

Fig. 26 Line plots of instantaneous nondimensional streamwise velocity measured for rigid canopy alone (a, d, g), rigid canopy with forebody (b, e, h), and periodic oscillating canopy with forebody (c, f, i), using URANS (a–c), LNS (d–f), and IDDES (g–i) turbulence models

The power spectral density of the fluctuating velocity component was calculated using the fast Fourier transform (FFT). The corresponding frequency (f_v) found from the FFT was converted to a nondimensional parameter, Strouhal number, $St = f_v D_P / U_\infty$. The computed power spectral density of fluctuating velocity for rigid canopy alone (a, d, g), rigid canopy with forebody (b, e, h) and periodic oscillating canopy with forebody (c, f, i), using URANS (a–c), LNS (d–f), and IDDES (g–i) turbulence models at each downstream location is presented in Fig. 27. For the rigid canopy alone configuration, all turbulence models show multiple low-frequency peaks in the wake, at approximately $St \approx 0.05$ and 0.15. These peaks for these frequencies increase approaching z* = 2, suggesting that the maximum peak is experienced at the downstream edge of the recirculating velocity region (i.e., streamlines of wake) as depicted in Fig. 14. The presence of the forebody increases the magnitude for the higher frequency (i.e., $St \approx 0.15$), while reducing the magnitude for the lower frequency peak (i.e., $St \approx 0.05$). For the periodic oscillation canopy configuration, the motion introduces a primary peak frequency in the velocity signal equal to the prescribed oscillation frequency (i.e., $St = 0.55$). Comparing turbulence models, the Hybrid RANS-LES models result in velocity

signals that are noisier than the URANS model, which explain multiple frequency peaks observed; however, the same frequencies (0.15, 0.55) are still observed.

These computed frequency peaks compare well to the experiment. The authors from the rigid canopy experiment found three distinct peaks corresponding to $St \approx 0.02$, 0.05, 0.07, and 0.15 within the same streamwise locations.[16] Berger et al.[30] measured a low-frequency peak at $St = 0.05$ in the near wake of a disk, which was due to the oscillation or pumping of the recirculation bubble. These results suggest that the lower frequency peak observed in simulation is the characteristic frequency of the recirculation region in the wake. The $St \approx 0.15$ peak correlates with the $St = 0.135$ value reported by both Berger et al.[30] and Fuchs e.[31] associated with helical vortex structures present downstream in the wake. Similarly found in the experiment, none of the rigid canopy configurations studied revealed a peak corresponding to the high-frequency peak exhibited by the flexible canopy at $St \approx 0.55$. The results indicate that the high-frequency peak (i.e., canopy breathing) is an outcome of FSIs and not a natural frequency of the rigid canopy.

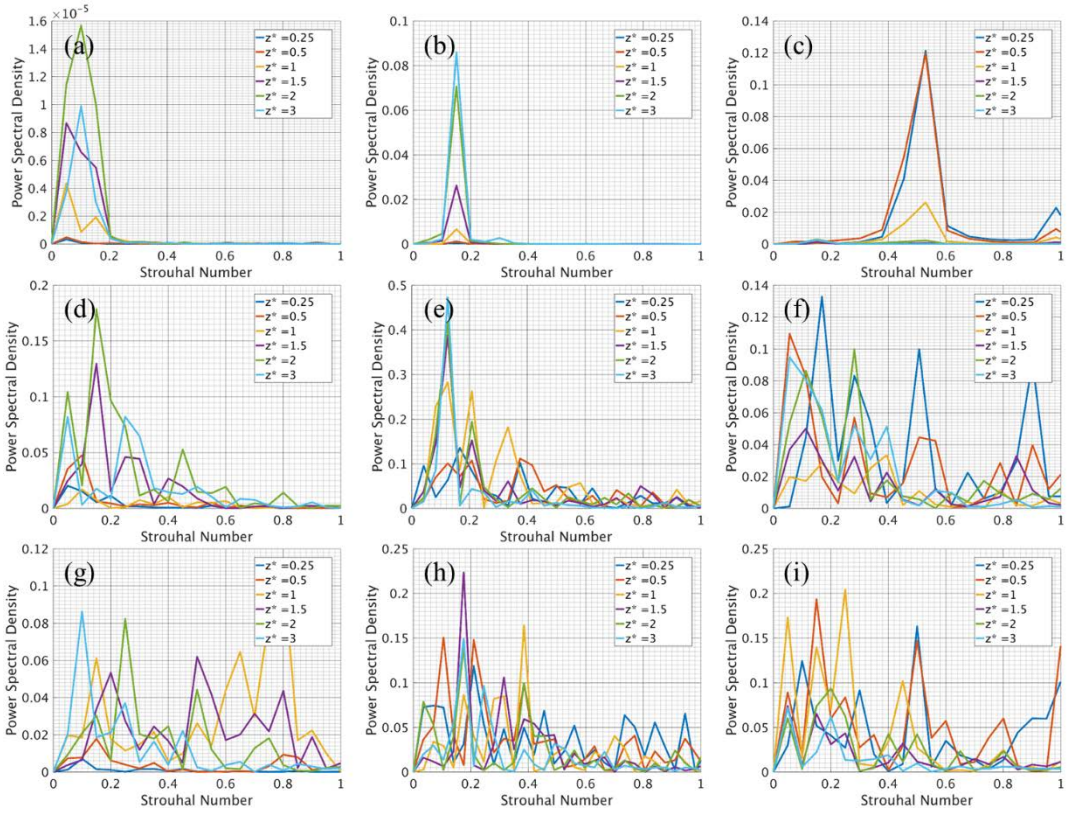

Fig. 27 Computed power spectral density of fluctuating velocity for rigid canopy alone (a, d, g), rigid canopy with forebody (b, e, h) and periodic oscillating canopy with forebody (c, f, i), using URANS (a–c), LNS (d–f), and IDDES (g–i) turbulence models

3.5 Permeability and Free-Stream Turbulence

Since the rigid canopy simulations exhibited substantially larger drag values than that of the flexible canopy, a parameter study was explored for both permeability of the canopy and free-stream turbulence levels. It was hypothesized that modeling permeability and promoting early transition on the surface of the canopy would result to lower drag values. Steady-state RANS CFD simulations were performed and were compared to the previous steady-state CFD simulation result of the baseline rigid canopy. The goal of the parameter study was to identify trends in drag and wake flow structure when compared to the baseline rigid canopy.

Permeability is characterized by an average velocity, *c*, across the canopy. The authors determined that the dimensionless permeability ratio, c/U_∞, of the flexible canopy used in the water tunnel experiment was approximately 1%–2%. To model the permeability, the top and bottom surfaces of the rigid canopy were set as wall bleed and suction surfaces, respectively. The bleed and suction rates were set equal and at a constant value. Two dimensionless permeability ratio values were simulated, c/U_∞ = 2% and 4%.

The effects of turbulence intensity and turbulent viscosity ratio were studied to determine if the instrumented forebody support structure upstream of the flexible canopy from water tunnel experiment affected the drag as well as the near wake flow of the canopy. Two separate simulations were performed without the presence of a forebody upstream: 1) the turbulence intensity level was increased to 9% and 2) the viscosity ratio was decreased to 10. It was hypothesized that increasing the turbulence intensity as well as decreasing the turbulent viscosity ratio would alter the wake flow structure due to the increase in turbulent kinetic energy and decrease in viscous dissipation in the flow. The drag coefficient was computed for each simulation using Equation 1, and is presented in Table 6.

Table 6 Drag coefficient for a rigid hemisphere only at different permeability ratios and free-stream turbulence parameters

Steady CFD (R k-ϵ)	$C_{D_{rigid}}$
Baseline (c/U_∞ = 0%, T_u = 3%, μ_T/μ = 50)	1.467
c/U_∞ = 2%, T_u = 3%, μ_T/μ = 50	1.434
c/U_∞ = 4%, T_u = 3%, μ_T/μ = 50	1.406
c/U_∞ = 0%, T_u = 9%, μ_T/μ = 50	1.474
c/U_∞ = 0%, T_u = 3%, μ_T/μ = 10	1.465

The parameter that had the largest effect in reducing drag was the permeability ratio. Predictably, the increase in permeability led to a further decrease in drag. The inflow near the top surface of the canopy reduces the overall velocity deficit, therefore resulting in a decrease in drag. Although the data set is limited, the results suggest that the permeability is approximately correlated linearly to drag reduction (i.e., $c/U_\infty = 4\%$ results in drag reduction of approximately 4%). The free-stream turbulent intensity and viscosity ratio had little to no effect on drag. Unlike solid spherical bluff bodies, the separation point for the rigid canopy is fixed at the canopy skirt and does not move along the surface downstream when the flow transitions to turbulent.[32] Therefore, the size of the wake is not reduced, and the drag remains relatively constant. Moreover, studies have shown that the drag coefficients of a parachute canopy are Reynolds number-independent for values greater than approximately 10^4.[24,33,34]

The streamwise velocity along centerline as a function of downrange distance from the canopy surface for the permeability and turbulent parameters is presented in Fig. 28. The axial velocity profile is able to provide quantitative insight into the size and magnitude of the wake near the canopy surface. As expected, the free-stream turbulent parameters had little to no effect on the development of the wake flow. Specifically, the peak velocity deficit is unchanged. However, the increase in turbulence intensity causes full velocity recovery sooner downstream than compared to the baseline. The permeable canopy allows flow to pass through the surface and introduce positive flow velocity into the near wake of the canopy. The inflow reduces the peak velocity deficit compared to the solid canopy. Increasing the permeability further reduces the peak velocity deficit. Interestingly, although the peak velocity deficit decreases, the wake of the permeable canopy is stretched, delaying full velocity recovery farther downstream. Therefore, the results suggest that the velocity deficit in the wake follows a type of conservation behavior (i.e., the total velocity deficit is conserved). Although modeling the surfaces of the canopy to be permeable reduced the drag, the simulation is still unable to explain the large discrepancy in drag between the rigid canopy and the flexible canopy from the experiment. Therefore, the results suggest that the combination of canopy dynamics, upstream geometry modeling (i.e., forebody or payload), and porosity of the canopy may be vital in accurately modeling the aerodynamics of parachute canopies.

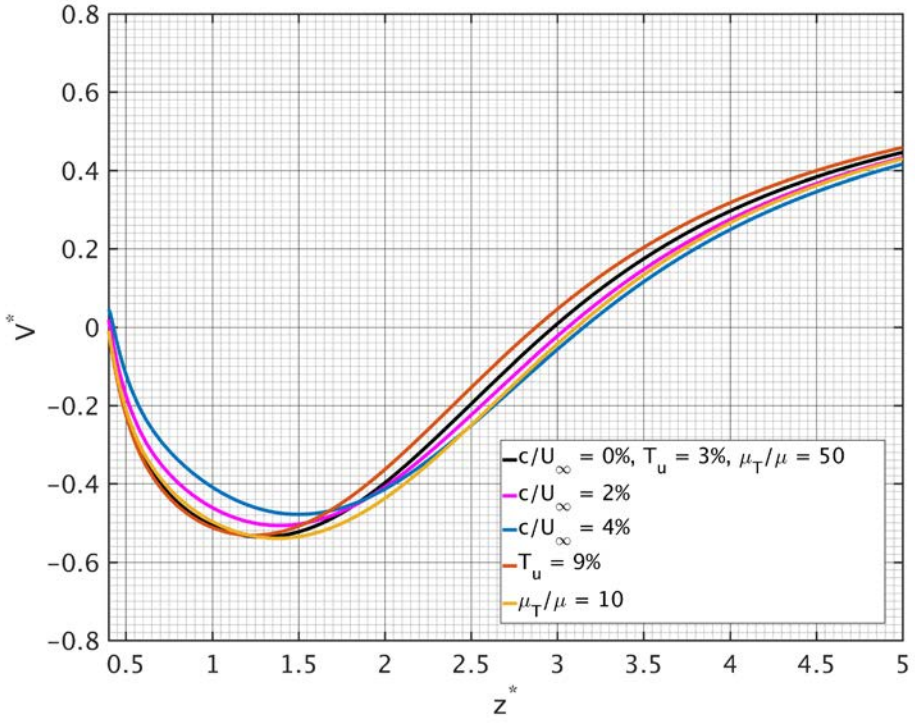

Fig. 28 Nondimensional streamwise velocity at x* = 0 as a function of downstream distance for a rigid canopy (black), canopy with (c/U_∞ = 2%) permeability (pink), and (c/U_∞ = 4%) permeability (blue), free-stream turbulence intensity (T_u = 9%) (orange), and a turbulent viscosity ratio (μ_T/μ = 10) (yellow). (rigid canopy only)

4. Conclusions

A computational study on the wake flow for a rigid body and periodic oscillating canopy with and without the presence of an upstream forebody was investigated in order to provide insight into what parameters in simulation (e.g., turbulence model) and canopy features (i.e., permeability and dynamics) produce the wake flow field that matches best to the experiment. A water tunnel test of a flexible canopy was used to help validate simulation results. Although the drag coefficient was significantly larger compared to the experiment, the prescribed periodic oscillating canopy with an upstream forebody yielded the largest effect in producing a wake flow that matched best to the experiment. The results show that modeling the upstream geometry or payload present is most critical followed by accurately modeling canopy dynamics. Furthermore, the Hybrid RANS-LES turbulence models best matched what was observed in the experiment and were able to resolve the flow structures that are present in the wake and the secondary flow structures near the surface of the canopy. The results indicate modeling the upstream geometry, canopy dynamics, and permeability of a canopy will lead to an accurate prediction of drag and the near wake flow field of a parachute canopy. Moreover,

the results underpin the importance of performing FSI investigations for parachute designs. Future work will focus on implementing coupled CFD–finite-element modeling codes to help model the FSIs of the fluid flow and structural dynamics of the flexible canopy.

5. References

1. Peterson CW, Strickland JH, Higuchi H. The fluid dynamics of parachute inflation. Annual Review of Fluid Mechanics. 1996;28:361–387.

2. Stein K, Benney R, Kalro V, Tezduyar T, Leonard J, Accorsi M. Parachute fluid-structure interactions: 3-D computation. Computer Methods in Applied Mechanics and Engineering. 2000;190:373–386.

3. Stein K, Benney R, Tezduyar T, Leonard J, Accorsi M. Fluid-structure interactions of a round parachute: modeling and simulation techniques. Journal of Aircraft. 2001;38(5):800–808.

4. Benney R, Stein K, Tezduyar T, Accorsi M, Zhang W, Leonard J. Fluid-structure interaction modeling of the US Army personnel parachute system. AIAA Modeling and Simulation Technologies Conference; 2000 Aug 14–17; Denver, CO. AIAA Paper No.: 2000-4310.

5. Tezduyar T, Sathe S, Keedy R, Stein K. Space-time finite element techniques for computation of fluid-structure interactions. Computer Methods in Applied Mechanics and Engineering. 2006;195:2000–2027.

6. Tezduyar T, Takizama K, Moorman C, Wright S, Christopher J. Space-time finite element computation of complex fluid-structure interactions. International Journal for Numerical Methods in Fluids. 2009;64:1201–1218.

7. Sahu J, Edge H, Heavey K, Stein K, Benney R, Chakravarthy S. Comparison of numerical flow field predictions for Army airdrop systems. Aberdeen Proving Ground (MD): Army Research Laboratory (US); 1999. Report No.: ARL-TR-1983.

8. Sahu J, Benney R. 3-D parachute descent analysis using coupled CFD and structural codes. 13th AIAA Aerodynamic Decelerator Systems Technology Conference; 1995 May 15–18; Clearwater Beach, FL. AIAA Paper No.: 95-1580.

9. Maydew RC, Peterson CW. Design and testing of high-performance parachutes. Neuilly-sur-Seine (France): Advisory Group for Aerospace Research and Development; 1991. Report No.: AGARD-AG-319.

10. Cruz JR, Mineck RE, Keller DF, Bobskill MV. Wind tunnel testing of various disk-gap-band parachutes. 17th AIAA Aerodynamic Decelerator Systems Technology Conference; 2003 May 19–22; Monterey, CA. AIAA Paper No.: 2003-2129.

11. Jenkins T, Desabrais K. Three-component velocity field measurements near a parachute during a drop test. 48th AIAA Aerospace Sciences Meeting; 2010 Jan 4–7; Orlando, FL. AIAA Paper No.: 2010-1030.

12. Lamberson D, Higuchi H, van Rooij M. Characteristics of flow within concave-nosed bodies. 15th AIAA Aerodynamic Decelerator Systems Technology Conference; 1999 June 8–11; Toulouse, France. AIAA Paper No.: 99-1738.

13. McQuilling M, Lobosky L, Sander S. Computational investigation of flow around a parachute model. 48th Journal of Aircraft. 2011;48(1):34–43.

14. Johari H, Desabrais KJ. Vortex shedding in the near wake of a parachute canopy. Journal of Fluid Mechanics. 2005;536:185–207.

15. Desabrais KJ, Johari H. Vortex shedding in the near wake of rigid and flexible bluff bodies. 44th AIAA Aerospace Sciences Meeting; 2006 Jan 9–12; Reno, NV. AIAA Paper No.: 2006-1307.

16. Desabrais KJ, Johari H. Vortex shedding in the near wake of three axisymmetric bluff bodies. Journal of Aircraft. 2017;54(6):2398–2401.

17. Metacomp Technologies, Inc. MIME user manual. Agoura Hills (CA): Metacomp; 2010.

18. Strickland JH, Higuchi H. Parachute aerodynamics: an assessment of prediction capability. Journal of Aircraft. 1996;33:241–252.

19. Desabrais KJ. Velocity field measurements in the near wake of a parachute canopy [PhD thesis]. [Worcester (MA)]: Worcester Polytechnic Institute; 2002.

20. Metacomp Technologies, Inc. CFD++ user manual, Agoura Hills (CA): Metacomp; 2011.

21. Batten P, Goldberg U, Chakravarthy S. LNS - an approach towards embedded LES. 40th AIAA Aerospace Sciences Meeting; 2002 Jan 14–17; Reno, NV. AIAA Paper No.: 2002-0427.

22. Shur ML, Spalart PR, Strelets MK, Travin AK. A hybrid RANS-LES approach with delayed-DES and wall modelled LES capabilities. International Journal of Heat and Fluid Flow. 2008;29:1638–1649.

23. Spalart PR, Allmaras SR. A one-equation turbulence model for aerodynamic flows. Recherche Aerospatiale. 1994;(1):5–21.

24. Hoerner SF. Fluid-dynamic drag. Bakersfield (CA): Hoerner Fluid Dynamics; 1965. Chap. 3.

25. Peterson CW, Johnson DW. Reductions in parachute drag due to forebody wake effects. Journal of Aircraft. 1983;20(1):42–49.

26. Sengupta A, Steltzner A, Witkowski A, Candler G, Pantano C. Findings from the supersonic qualification program of the Mars Science Laboratory parachute system. 20th AIAA Aerodynamic Decelerator Systems Technology Conference and Seminar; 2009 May 4–7; Seattle, WA. AIAA Paper No.: 2009-2900.

27. McQuilling M, Potvin J. Forebody wake effects on the aerodynamics of an annular parachute. 42nd AIAA Fluid Dynamics Conference and Exhibit; 2012 June 25–28; New Orleans, LA. AIAA Paper No.: 2012-3332.

28. Heinrich HG, Riabokin T. Analytical and experimental consideration of the velocity distribution in the wake of a body of revolution. Wright Patterson Air Force Base (OH): Wright Air Development Division Report; 1959. Report No.: WADD 60-257.

29. Heinrich HG, Eckstrom DJ. Velocity distribution in the wake of bodies of revolution based on drag coefficient. Air Force Flight Dynamics Laboratory; 1963. Report No.: TDR-62-1103.

30. Berger E, Scholz D, Schumm M. Coherent vortex structures in the wake of a sphere and a circular disk at rest and under forced vibrations. Journal of Fluids and Structures. 1990;4:231–257.

31. Fuchs HV, Mercker E, Michel U. Large-scale coherent structures in the wake of axisymmetric bodies. Journal of Fluid Mechanics. 1979;93:185–207.

32. Achenbach E. Experiments on the flow past spheres at very high Reynolds numbers. Journal of Fluid Mechanics. 1972;54:565–575.

33. Knacke TW. Parachute recovery systems design manual. Santa Barbara (CA): Para Publishing;1992 Mar. Report No.: NWC-TP-6575.

34. Cockrell DJ. The aerodynamics of parachutes. Neuilly-sur-Seine (France): Advisory Group for Aerospace Research and Development; 1987. Report No.: AGARD-AG-295.

Nomenclature

D_0	=	constructed canopy diameter
D_p	=	time-averaged projected canopy diameter
H	=	depth of canopy
δ	=	thickness of canopy
U_∞	=	free-stream velocity
Re_{Dp}	=	free-stream Reynolds number based on D_p
D_{fb}	=	forebody diameter
H_{fb}	=	length of forebody
L	=	distance from forebody to base of canopy
f_b	=	breathing frequency of canopy oscillation
ϕ	=	phase angle of canopy oscillation
x_0	=	nominal spanwise coordinate of control point
y_0	=	nominal cross-stream coordinate of control point
z_0	=	nominal streamwise coordinate of control point
x_{max}	=	maximum spanwise coordinate of control point
y_{max}	=	maximum cross-stream coordinate of control point
z_{max}	=	maximum streamwise coordinate of control point
x_{min}	=	minimum spanwise coordinate of control point
y_{min}	=	minimum cross-stream coordinate of control point
z_{min}	=	minimum streamwise coordinate of control point
Δt	=	global simulation time step
St	=	Strouhal number
C_{Drigid}	=	rigid canopy drag coefficient
D	=	drag force
ρ_∞	=	free-stream density
S	=	cross-sectional area based on D_p
C_D	=	drag coefficient of parachute canopy with a forebody present
$C_{D,\infty}$	=	drag coefficient of parachute canopy without a forebody present

u = streamwise velocity component

C_{Dfb} = drag coefficient of forebody

$Drag_{fb}$ = drag force of forebody

S_{fb} = cross-sectional area based on D_{fb}

x = spanwise coordinate

C_{Dflex} = drag coefficient of flexible canopy

C_{Dpo} = drag coefficient of periodic oscillating canopy

C_P = nondimensional pressure coefficient

p = static pressure

p_∞ = free-stream pressure

x^* = nondimensional spanwise coordinate

y^* = nondimensional cross-stream coordinate

z^* = nondimensional streamwise coordinate

V^* = nondimensional streamwise velocity component

Ω^* = nondimensional out-of-plane vorticity

Q^* = nondimensional Q-criterion

f_v = computed frequencies from FFT of velocity fluctuations in wake

c/U_∞ = permeability ratio

T_u = turbulence intensity

μ_T/μ = turbulent viscosity ratio

t = global time

List of Symbols, Abbreviations, and Acronyms

3-D	3-dimensional
CFD	computational fluid dynamics
CFL	Courant-Friedrichs-Lewy
DOD	Department of Defense
DSRC	DOD Supercomputing Resource Center
FFT	fast Fourier transform
FSI	fluid-structure interaction
IDDES	Improved Delayed Detached Eddy Simulation
LES	large-eddy simulation
LNS	Metacomp's Batten-Goldberg Hybrid RANS-LES
MIME	Multipurpose Intelligent Meshing Environment
PDV	planar Doppler velocimetry
RANS	Reynolds-averaged Navier-Stokes
R k-ϵ	realizable k-ϵ
RBF	radial basis functions
URANS	unsteady RANS

1 (PDF) DEFENSE TECHNICAL INFORMATION CTR DTIC OCA

2 (PDF) DIR ARL
IMAL HRA
RECORDS MGMT
RDRL DCL
TECH LIB

1 (PDF) GOVT PRINTG OFC
A MALHOTRA

1 (PDF) ARL
RDRL WML E
J VASILE